Buckling and Topological Defects in Graphene and Carbon Nanotubes

by

Shuo Chen

A dissertation submitted in partial satisfaction of the
requirements for the degree of
Doctor of Philosophy

in

Engineering – Materials Science and Engineering

in the

Graduate Division

of the

University of California, Berkeley

Committee in charge:

Professor Daryl C. Chrzan, Chair
Professor John W. Morris, Jr.
Professor Sanjay Govindjee

Fall 2012

Buckling and Topological Defects in Graphene and Carbon Nanotubes

Abstract

Buckling and Topological Defects in Graphene and Carbon Nanotubes

by

Shuo Chen

Doctor of Philosophy in Engineering – Materials Science and Engineering

University of California, Berkeley

Professor Daryl C. Chrzan, Chair

Graphene is the strongest material ever discovered and has an extremely high Young's modulus ($\sim$ 1 GPa). Although stretching the sp^2 covalent bonds between carbon atoms is very difficult, significant deflections do develop in graphene membranes. In fact, thermal rippling naturally emerges in graphene at any finite temperature. Moreover, the topological defects mediating plastic deformation often cause out–of–plane crumpling, an effective way to reduce the total elastic energy of the topological defect. It is even possible to design specific stress states to produce periodic wrinkles in graphene with adjustable wave lengths.

This work aims to understand how buckling influences the elastic and plastic behavior of graphene–based nanostructures. While the elastic moduli may be straightforwardly computed using structure optimization techniques with applied test stresses, it is a nontrivial task to obtain elastic properties at any specific temperature. Further, linear elastic theories are not able to describe large buckling because the second order nonlinear terms in the definition of the Lagrangian finite strain tensor cannot be neglected. In addition, the existence of topological defects and constraints need to be properly treated. Finally, buckling and defects of a curved surface such as a nanotube is even more complicated and poses other intriguing challenges.

To proceed, we employ Monte Carlo techniques to obtain fundamental elastic properties of graphene at desired temperatures, which supplies useful inputs for a nonlinear continuum model for graphene. This model not only takes into account, in a suitable manner, both large out-of-plane buckling and interactions among edge dislocations with periodic boundary conditions, but also serves as a handy tool for simulating nanoindentation experiments and the controlled wrinkling of graphene. At last, we focus on the Stone–Wales defect mediated plasticity of CNTs. Specifically, a kinetic Monte Carlo framework is designed to model the defect dynamics over a long time scale. We find that in large nanotubes, a chain of closely packed dislocations (called a "dislocation worm") may have less buckling and lower formation energy than the conventional dislocation glide under high tensile stresses.

To my parents.

Contents

List of Figures

List of Tables

Acknowledgments

I would like to express my deepest gratitude to my advisor and mentor Professor Daryl C. Chrzan. His wisdom, knowledge and rigorous scientific attitudes have impressed and benefited me tremendously. Without his guidance, advice and encouragement, I would never finish this work. I am honored and proud to be one of his students.

Special thanks to Professor Elif Ertekin. She has given me many insightful suggestions and I learnt a lot from her.

I am grateful to Professor John W. Morris, Professor Sanjay Govindjee, Proessor Mark D. Asta and Professor Andrew Minor for serving as my committee members even at hardship.

Many thanks to the former COINS director Professor Jeffrey C. Grossman and the current director Dr. William Mickelson for supervising my research in COINS.

Lastly, my biggest thanks to my dear family. Their support, care and love consist of the most essential part of my life.

Chapter 1

Introduction

1.1 Motivations and Background

Recently, much research attention has been focused on graphene and carbon nanotubes (CNTs) due to their many unique and interesting properties. They are important members of the fullerene family which generally refers to macromolecules made of covalently bonded sp^2 carbon atoms, for example, the famous buckyball (C_{60}) whose structure resembles a soccer ball with the truncated icosahedron pattern. Fig. 1.1 shows the trend of public interest in graphene and carbon nanotubes using the search volume data for the keywords "carbon nanotubes" and "graphene" collected through the Google search engine (*www.google.com*). It is observed that while CNTs remain to be actively studied, graphene quickly draws lots of attentions and becomes a hot research topic starting in 2007.

Graphene is a single layer of sp^2–bonded carbon atoms densely packed in a honeycomb structure that can be abstracted as a two–dimensional (2D) hexagonal lattice. A (single–walled) carbon nanotube may be conceptually constructed by rolling up a graphene sheet into a cylinder along some specific lattice vector $\mathbf{l}$ that determines the chirality of the nanotube. For instance, in Fig. 1.2, assuming $\mathbf{a_1}$ and $\mathbf{a_2}$ are base vectors for a hexagonal lattice and $\mathbf{l} = m\mathbf{a_1} + n\mathbf{a_2}$ where m and n are integers, then rolling up the graphene along $\mathbf{l}$ produces a CNT whose chirality $\chi = (m, n)$. A zigzag CNT has $\chi = (m, 0)$ while an armchair one has $\chi = (m, m)$. The axis $\mathbf{h}$ of the nanotube may be written as $\mathbf{h} = m'\mathbf{a_1} + n'\mathbf{a_2}$ and the requirement $\mathbf{h} \cdot \mathbf{l} = 0$ leads to

$$m'(2m + n) + n'(2n + m) = 0. \tag{1.1}$$

In particular, for a zigzag CNT, $2m' + n' = 0$ and for an armchair one, $m' + n' = 0$. If periodic boundary conditions are imposed along the tube axis, then it is necessary that $\mathbf{h}$ be a lattice vector (*i.e.* m' and n' be integers). The geometrical relationships discussed above are useful to generate (pristine) CNTs for other simulation tasks.

The graphene lattice interconnected through covalent bonds between carbon atoms is extremely strong as it has been shown that the Young's modulus of graphite is around 1

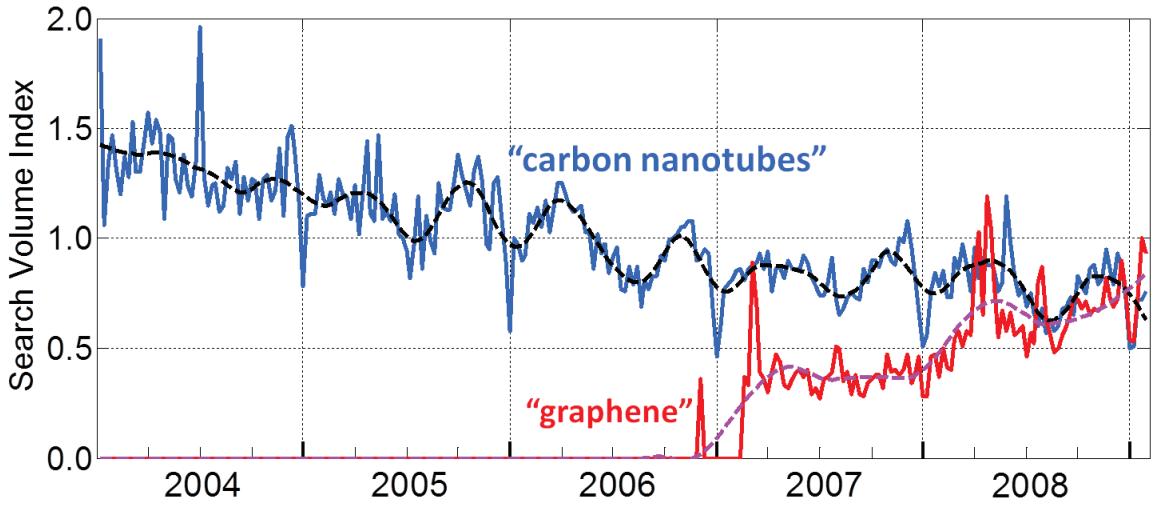

Figure 1.1: The search volume indices for the keywords "carbon nanotubes" and "graphene". The actual data (solid lines) are collected through *www.google.com* and the trends (dashed lines) are estimated using local regression methods. The data are scaled to the average search volume (ASV) of the keyword "carbon nanotubes" from 2004 to 2008. In this period, the ASV of "graphene" is 0.21 times the ASV of "carbon nanotubes".

GPa [44, 63]. In fact, graphene is widely accepted as the thinnest (one atom thick) and yet the strongest material ever discovered. Although it seems difficult to stretch graphene through in–plane tensile stresses, it is relatively easy to make a graphene membrane buckle out–of–plane. In this dissertation, we are mainly concerned with two types of buckling (Fig. 1.3), one is known as the thermal rippling which occurs at any finite temperature and the other one is the buckling induced by topological defects during plastic deformations. As we will explore in detail in the following chapters, buckling is intrinsically a highly nonlinear phenomenon that profoundly influences not only the elastic properties of graphene based structures such as the effective elastic moduli and thermal expansion but also the plastic behavior through effective screening of defect interactions.

According to the Mermin–Wagner theorem [33], at any finite temperature, the spontaneously developed out–of–plane thermal fluctuations will eventually destroy the long–range translational symmetry of the 2D hexagonal lattice of graphene. Therefore, graphene, as a 2D crystal, should not exist in the thermodynamic limit. However, a graphene flake is still well defined, but contains significant thermal ripples, as shown in the left panel of Fig. 1.3 where a 25.56 Å × 24.60 Å graphene sheet with 240 atoms naturally crumples at about 3500 K with an average deflection around 0.8 Å.

A well known example of topological defects in graphene (and other fullerenes) is the Stone-Wales defect [52] that can be created by rotating a single carbon–carbon bond ap-

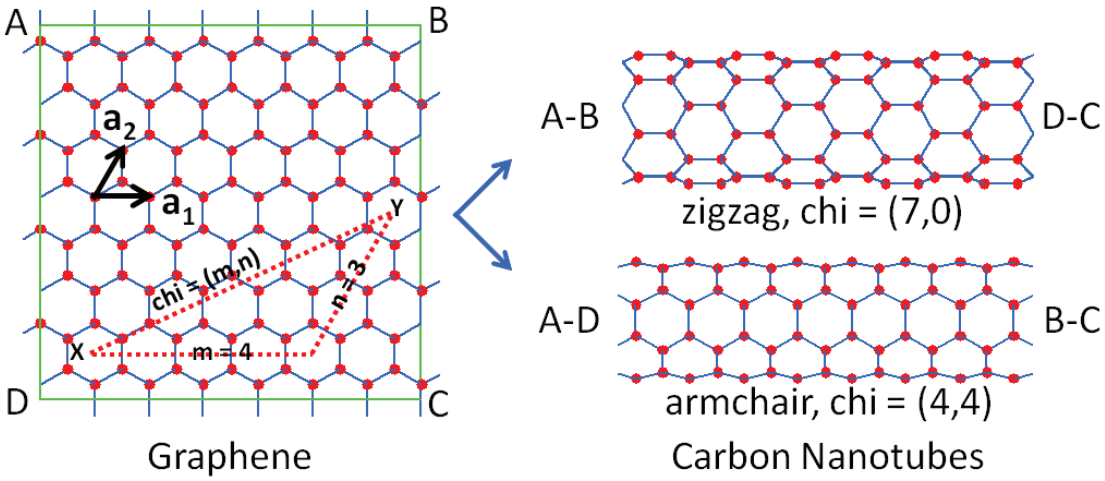

Figure 1.2: The structure of a monolayer graphene sheet (left) which can be wrapped into a zigzag CNT (top right), an armchair CNT (bottom right) or CNTs with other chiralities. The base vectors $\mathbf{a_1}$ and $\mathbf{a_2}$ define a two–dimensional hexagonal lattice.

proximately 90 degrees (breaking old bonds and/or forming new bonds if necessary). A Stone–Wales defect consists of a pair of topological defects (identified as dislocations below), each of which is composed of a pentagon and a neighboring heptagon. As illustrated in the top panel of Fig. 1.4, rotating another bond at the shoulder of one heptagon will separate this pair of topological defects by one lattice parameter $a = 2.46$ Å. In the continuum limit (the bottom panel of Fig. 1.4), a bond rotation may be regarded as opening a cut in the membrane and then displacing one edge of the cut by a relative to the other edge, producing a pair of dislocations of opposite sign. The length of the Burgers vector of each dislocation is $b = a = 2.46$ Å.

1.2 Outline

Chapter 2 discusses the thermal rippling and elastic properties of graphene. Besides several useful temperature dependent relationships derived from Monte Carlo simulations and rigorous fluctuation formulas, we emphasize how the system size impacts the magnitude of thermal fluctuations, the elastic compliances and other thermodynamic functions.

Chapter 3 presents a general nonlinear continuum theory for buckled edge dislocations in a thin film with periodic boundaries. In particular, this theory is applied to compute dislocation formation energies and the surface morphology of a free–standing graphene membrane. The knowledge of elastic moduli of graphene obtained from Chapter 2 provides essential in-

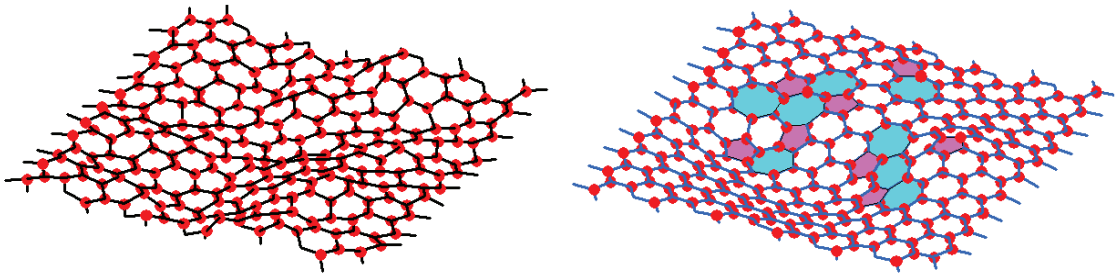

Figure 1.3: The thermal buckling (left) and the defect induced buckling (right) of a finite sized free–standing graphene with periodic boundaries.

put parameters for the continuum model. It is shown that the dislocation formation energy is effectively brought down through out–of–plane buckling and approaches a well defined (but very high) value ~ 6 eV in the thermodynamic limit. Thus, just like vacancies, a finite density of dislocations is expected at any strictly positive temperature, which, according to the 2D melting theory [17], implies that an infinitely large graphene sheet has a melting point of 0 K.

Having studied dislocations in graphene, Chapter 4 focuses on topological defects in CNTs and explores how buckling, tube dimensions and applied stresses together determine the energetically favored defect pattern and the dynamics of plastic deformations. It is proposed that under certain conditions, the plasticity of CNT is mediated through a line of side by side Stone-Wales defects (named a "dislocation worm") instead of dislocation glide because of a subtle tradeoff between the buckling energy and the dislocation core energy.

Chapter 5 briefly reviews important results and points out possible directions for the future work.

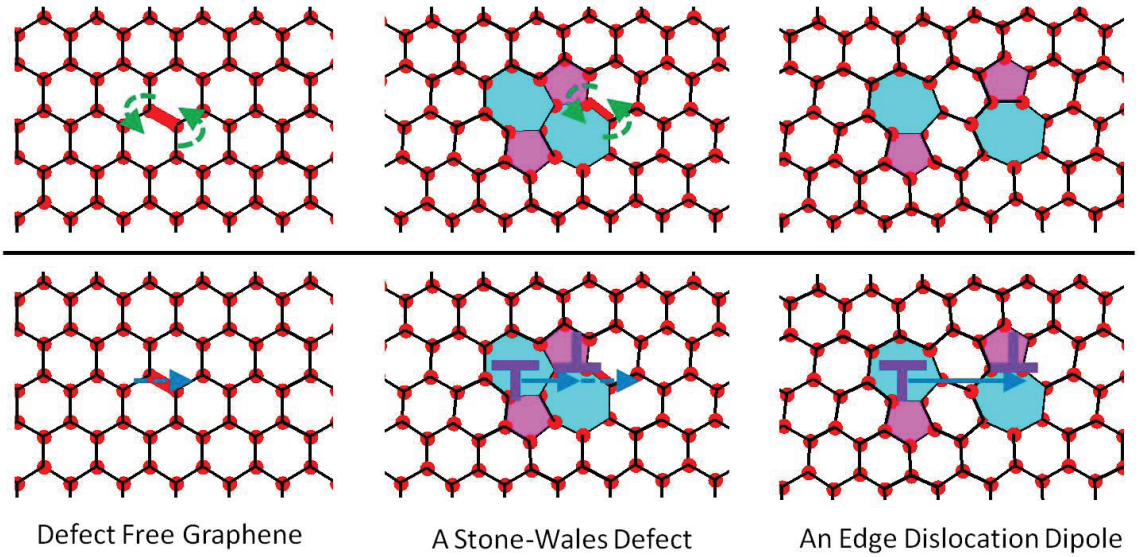

Figure 1.4: The nucleation of a Stone–Wales defect and then a dislocation dipole in the atomistic picture (top) or the continuum picture (bottom). The combination of a pentagon and a neighboring heptagon can be identified as an edge dislocation.

Chapter 2

Elastic Properties of Graphene

2.1 Introduction

The mechanical properties of graphene have already been considered theoretically. Lier and coworkers computed Young's modulus and Poisson's ratio for carbon nanotubes and graphenes at 0 K by stress relaxation at fixed distortions using density functional theory based methods [56]. Mounet and collaborators obtained the phonon spectrum of graphene at different lattice parameters through an *ab initio* method and then applied the quasi-harmonic approximation (QHA) to derive the free energies, the equilibrium lattice parameters and the elastic moduli as a function of temperature [37]. At higher temperatures, the elastic constants can be extracted directly from a Monte Carlo (MC) simulation without invoking the QHA by averaging the elastic responses of carbon sheets to small deformations for a number of sampled configurations [62]. It is also possible to model a carbon membrane as a thin plate and relate its Young's modulus with the vibration modes under appropriate boundary conditions [24].

In this chapter, the elasticity of stress–free graphenes at several temperatures is studied using Monte Carlo (MC) techniques with the isoenthalpic–isotension–isobaric (HtN) ensemble [15]. An obvious advantage to working in the HtN ensemble is that the elastic compliance, the thermal expansion coefficient, the heat capacity and many other interesting thermodynamic functions can be derived rigorously from the statistics of (finite) strains and kinetic energies [45] and thus are independent of the QHA. This approach has been applied successfully to three-dimensional bulk materials, (*e.g.*, silicon [25]) and with simple modifications can be applied in two-dimensional systems.

Our simulations confirm that a single-layered graphene may spontaneously develop thermal ripples at finite temperatures [14, 34]. These ripples soften the elastic moduli effectively in the sense that stretching a crumpled graphene sheet requires less force than stretching a flat one. Furthermore, the predicted thermal expansion coefficient assume a very small or even negative value at low temperatures, in accord with recent experiments [1].

2.2 Simulation Methods

2.2.1 HtN Ensemble

The general framework of Metropolis MC using the HtN ensemble [16, 15] is employed as follows. A flat, nearly square shaped monolayer graphene of N atoms is taken as the initial configuration. Using three-dimensional Cartesian coordinates, the graphene membrane lies in the x–y plane and periodic boundary conditions are imposed. The periodic supercell is represented by a two by two matrix h, each column of which defines an edge of the box. One MC step consists of, on average, N trials of moving a randomly selected atom in the three-dimensional space plus one trial of changing the shape of the simulation box. When the system is subjected to zero external pressure and zero thermodynamic tension, the acceptance probability for a random perturbation follows [16]:

$$\min\left\{1, \quad \left(\frac{A'}{A}\right)^N \left(\frac{H - U(r'_N)}{H - U(r_N)}\right)^{3N/2-1}\right\} \tag{2.1}$$

where H is the constant enthalpy of the system, $A = \det(h)$ is the projected area of the carbon membrane in the x–y plane, $U(r_N)$ is the potential energy computed through the classical REBO potential [4], r_N refers to the all the coordinates of N atoms, and the quantities with and without primes correspond to the new and old configurations respectively. The step size for each trial move is around 0.1 Å and is chosen adaptively depending on the specified boundary conditions such that the acceptance probability is close to 50%.

Two cases are considered. In one case (call it *case 2D*), all atoms are confined in the x–y plane but in the other case (call it *case 3D*), atoms are allowed to move in the z direction to produce out–of–plane thermal fluctuations. In each case, simulations are performed for six system sizes, namely, $N = 60, 112, 240, 448, 836, 1560$, and the enthalpies examined range from -7.30 eV/atom to -6.20 eV/atom. A typical simulation runs 4×10^6 MC steps for case 2D or 20×10^6 MC steps for case 3D. The first 1×10^6 steps and the remaining steps are used to, respectively, obtain the thermal equilibrium state and compute various interested statistics. The statistical errors are estimated from two stochastically independent MC simulations.

The in–plane finite strain tensor ε is defined in terms of the h matrix [46], namely, $\varepsilon = (\tilde{J}J - I)/2$ where $J = hh_0^{-1}$ is the Jacobian matrix, h_0 corresponds to an undeformed reference configuration, I is the two by two identity matrix and the tilde denotes the transpose of a matrix. The thermodynamic tension t is associated with the in–plane stress tensor σ by [46] $t = (A/A_0)J^{-1}\sigma\tilde{J}^{-1}$ where $A = \det(h)$ and $A_0 = \det(h_0)$. For stress–free graphene, σ (and thus t) is fixed to zero. Fig. 2.1 summarizes the above settings.

Following Graben and Ray [16], the temperature T of the system can be evaluated through $\langle K \rangle = 3Nk_BT/2$ where the kinetic energy $K = H - U(r_N)$ and k_B is the Boltzmann constant.

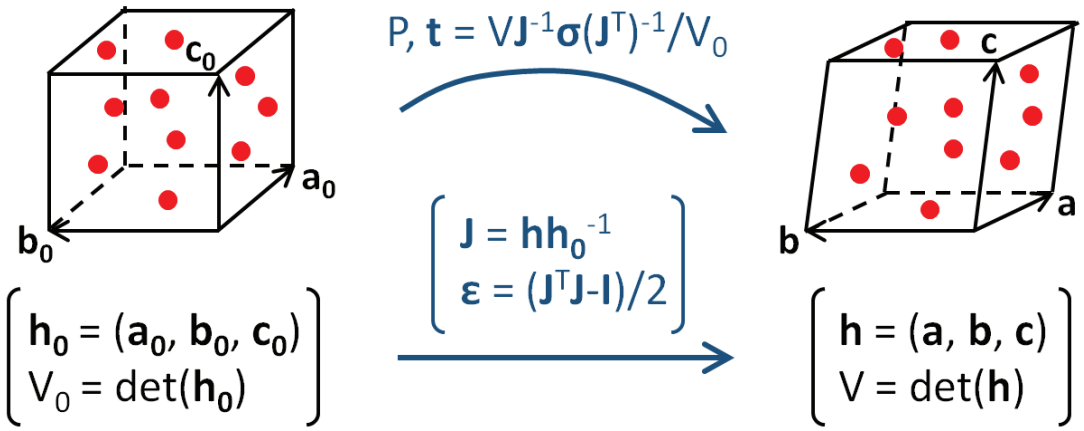

Figure 2.1: The setup of MC simulations within the HtN ensemble for anisotropic solids.

2.2.2 Fluctuation Formulas

The heat capacity at zero stress $C_t = T(\partial S/\partial T)_t$, the thermal strain tensor $\beta_{ij} = (\partial \varepsilon_{ij}/\partial T)_t$ and the *adiabatic* elastic constant $c^S_{ijkl} = (\partial t_{kl}/\partial \varepsilon_{ij})_S$ are readily available using fluctuation formulas [45]:

$$\langle K^2\rangle - \langle K\rangle^2 = \frac{3}{2}N(k_BT)^2(1 - \frac{3Nk_B}{C_t}) \tag{2.2}$$

$$\langle \varepsilon_{ij}K\rangle - \langle \varepsilon_{ij}\rangle\langle K\rangle = -\frac{3}{2}N(k_BT)^2\frac{\beta_{ij}}{C_t} \tag{2.3}$$

$$\langle \varepsilon_{ij}\varepsilon_{kl}\rangle - \langle \varepsilon_{ij}\rangle\langle \varepsilon_{kl}\rangle = \frac{k_BT}{A_0}(c^S)^{-1}_{ijkl} \tag{2.4}$$

It is a standard exercise to derive the heat capacity at zero strain $C_\varepsilon = T(\partial S/\partial T)_\varepsilon$, the thermal stress tensor $b_{ij} = (\partial t_{ij}/\partial T)_\varepsilon$ and the *isothermal* elastic constant $c^T_{ijkl} = (\partial t_{ij}/\partial \varepsilon_{kl})_T$, for instance [59],

$$C_\varepsilon = C_t/(1 + \frac{A_0T}{C_t}\beta_{ij}\beta_{kl}c^S_{ijkl}) \tag{2.5}$$

$$b_{ij} = -\frac{C_\varepsilon}{C_t}c^S_{ijkl}\beta_{kl} \tag{2.6}$$

$$c^T_{ijkl} = c^S_{ijkl} - \frac{A_0T}{C_\varepsilon}b_{ij}b_{kl}. \tag{2.7}$$

Given the elastic constant matrix c (and thus the elastic compliance matrix $s = c^{-1}$), the

in–plane Young's modulus, shear modulus and Poisson's ratio are calculated through

$$Y = 2/(s_{1111} + s_{2222}) \tag{2.8}$$
$$G = 1/(4s_{1212}) \tag{2.9}$$
$$\nu = -s_{1122}/Y. \tag{2.10}$$

Note that Y, G and ν as defined above must be understood in an average sense. In this paper both Y and G have the unit eV/Å^2, respecting the two–dimensional nature of graphene (1.00 eV/Å^2 corresponds to 47.76 GPa assuming the interlayer distance of 3.35 Å in graphite).

2.3 Results and Discussions

2.3.1 Thermal Rippling

Significant out-of-plane fluctuations are observed in all simulations. In particular, Fig. 2.2 shows two snapshots of a crumpled graphene consisting of 1560 atoms in the thermal equilibrium state with the enthalpy fixed to be either -7.30 eV/atom or -6.20 eV/atom. The maximal amplitude of the thermal ripples can reach as large as ~ 4.0 Å at a high temperature (in comparison, the bond length of graphene is about 1.42 Å). The rippling gives rise to a nontrivial bending strain field [28] $F_{ij} = (1/2)\partial_i z \partial_j z$ whose spatial average is given by $\bar{F}_{ij} = (1/A)\int F_{ij}\,\mathrm{d}x\mathrm{d}y$ where i, j can be either x or y. (The bending strain will play an important role in constructing our continuum theory for buckled graphene in the next chapter.) Given the atom positions of a wrinkled graphene sheet, it is not hard to construct the surface morphology $z(x, y)$ through interpolation and then $\bar{F}_{ij}$ can be numerically evaluated. It is found that the thermal rippling results in a nearly spherical bending strain, *i.e.* $\bar{F}_{ij} = \bar{F}\delta_{ij}$, and $\bar{F}$ varies from $\sim 0.27\%$ (the top panel of Fig. 2.2) to $\sim 5.65\%$ (the bottom panel of Fig. 2.2).

Another way to characterize the thermal fluctuations is to look at the standard deviation of the out–of–plane atom displacements D_z versus that of the in–plane atom displacements D_{xy}, as demonstrated in Fig. 2.3. An immediate observation is that D_z is significantly greater than D_{xy} for all temperatures we have examined. In addition, at the same temperature, D_z clearly increases with the system size whereas D_{xy} exhibits a much weaker size dependence. It can be further shown that D_{xy} slightly drops (about 10%) when the thermal rippling is manually turned off (case 2D), which may be explained by the coupling between the rippling and the stretching modes in a two–dimensional membrane [42]. If such coupling can be ignored, it may be deduced from the harmonic approximation that [42] $\langle|z(\mathbf{q})|^2\rangle \propto k_B T/(\kappa \mathbf{q}^4)$ for a stress–free sheet where $z(\mathbf{q})$ is the Fourier component of $z(x, y)$, κ is the bending rigidity. Since the main contribution to D_z comes from $z(\mathbf{q})$ with small $|\mathbf{q}|$ (the long wavelength components), D_z should be approximately proportional to T, which is the case for $T >\sim 1000$ K. The increased D_z in large systems may lead to a very small or even negative thermal expansion coefficient β (Fig. 2.4). In case 2D, β has virtually no size dependence and remains

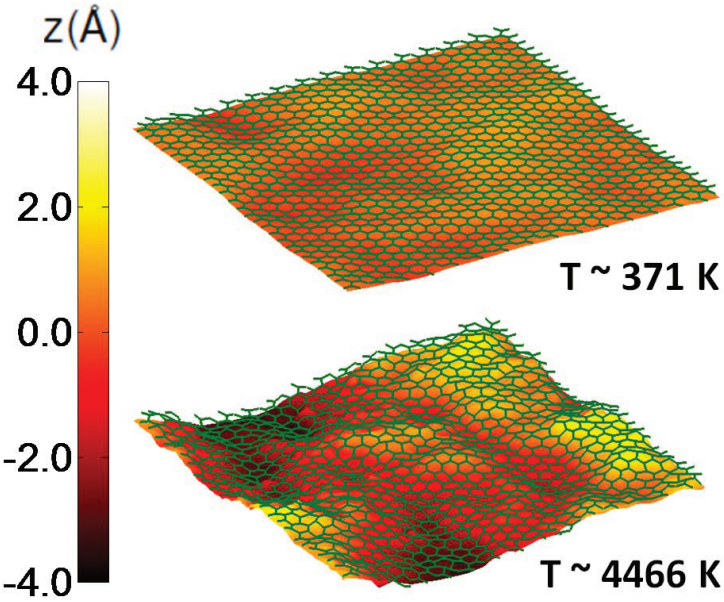

Figure 2.2: Snapshots of a wrinkled graphene with 1560 carbon atoms extracted from HtN MC simulations. Each snapshot displays both the network of sp^2 bonds of graphene and the corresponding interpolated surface morphology. In the top panel, the enthalpy H is fixed to be -7.30 eV/atom (~ 371 K), while in the bottom panel, $H = -6.20$ eV/atom (~ 4466 K).

positive, while in case 3D, β continuously decreases as the system size increases and reaches the value $\sim -1.92 \times 10^{-7}$ for $N = 1560$ and $H = -7.30$ eV/atom (~ 371 K). It appears that β will be further reduced as the thermodynamic limit is approached.

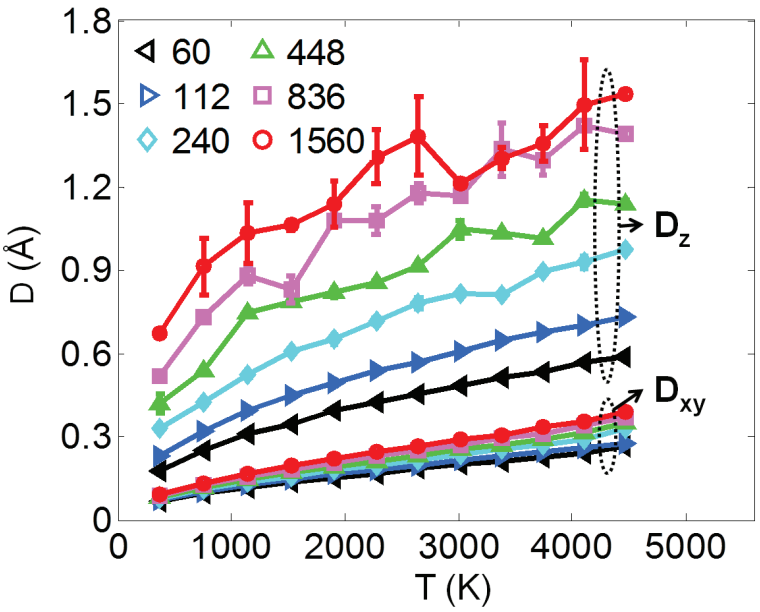

Figure 2.3: The standard deviation of the out–of–plane displacements D_z and that of the in–plane displacements D_{xy} as a function of temperature for different system sizes.

The thermal expansion coefficient is closely related to the lattice parameter a as a function of temperature. We differentiate two types of lattice parameter in accordance with the fact that the graphene sheet is significantly crumpled. The internal lattice parameter a_{int} associated with the average sp^2 bond length indicates the actual size of the system, while the external lattice parameter a_{ext} computed from the dimension of the 2D simulation box tells the effective size of the system, which can be, at least in principle, straightfowardly measured through experiments. Fig. 2.5 displays a_{int} and a_{ext} for various system sizes at different temperatures. The internal lattice parameter shows no obvious size dependence and grows linearly with temperature, which behaves like conventional bulk materials. However, be aware that the 3D case corresponds to a larger $\mathrm{d}a_{\text{int}}/\mathrm{d}T$ than the 2D case because the bond has more degrees of freedom for stretching in case 3D. Notice that the thermal expansion coefficient $\beta(T)$ is proportional to $\mathrm{d}a_{\text{ext}}/\mathrm{d}T$. Therefore, similarly to Fig. 2.4, we observe strong size dependence of $a_{\text{ext}}(T)$ for case 3D but no such size dependence for case 2D. It should be pointed out that $\beta(T)$ in Fig. 2.4 is calculated through evaluating the cross variation of the strain tensor and the kinetic energy based on the fluctuation formula Eq. 2.3 rather than directly taking numerical derivatives of $a_{\text{ext}}(T)$.

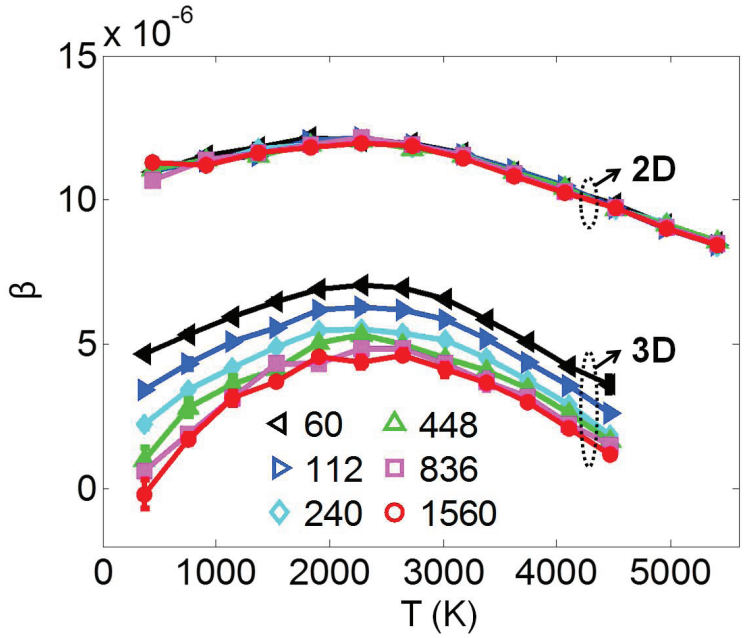

Figure 2.4: The linear thermal expansion coefficient β calculated using HtN MC simulations.

2.3.2 Elastic Moduli

The adiabatic and isothermal Young's modulus, shear modulus can be easily calculated from the fluctuation of strains according to Eq. (2.4) and (2.7). Fig. 2.6 summarizes the main results. In general, both Y and G decrease as the temperature increases, which may be simply explained using the Varshni model [58]. In addition, the presence of thermal ripples reduces the elastic moduli and such reduction increases with the system size. For instance, for $N = 1560$ and $H = -7.30$ eV/atom (~ 371 K), the artificially flattened graphene (case 2D) has $Y_S \sim 18.63$ eV/Å^2 ~ 0.8900 TPa which agrees with the density functional theory based calculations [56], while the crumpled graphene (case 3D) has $Y_S \sim 12.51$ eV/Å^2 ~ 0.5973 TPa, showing a reduction of Y_S over 30%. This modulus softening effect due to the thermal rippling can be understood qualitatively as follows: the evident out–of–plane crumpling of graphene (see Fig. 2.2) effectively folds the membrane. Therefore, an infinitesimal test stress must unfold the membrane first and this unfolding does not stretch many covalent bonds as in the case of pulling a nearly flat graphene. In other words, while case 2D reflects the true strength of a network of bonded carbon atoms, case 3D only tells the strength of a folded network because the strains in Eq. (2.4) do not include the bending components F_{ij}. However, since thermal rippling always exist in a free–standing graphene at any finite temperature, the real experiments may be more faithfully simulated by case 3D. If one is more interested in the isothermal elastic moduli such as Y_T and G_T, Eq. 2.7 can be applied. Y_T is found to be smaller than Y_S but the difference is small ($< 5\%$ for case 2D and $< 1\%$

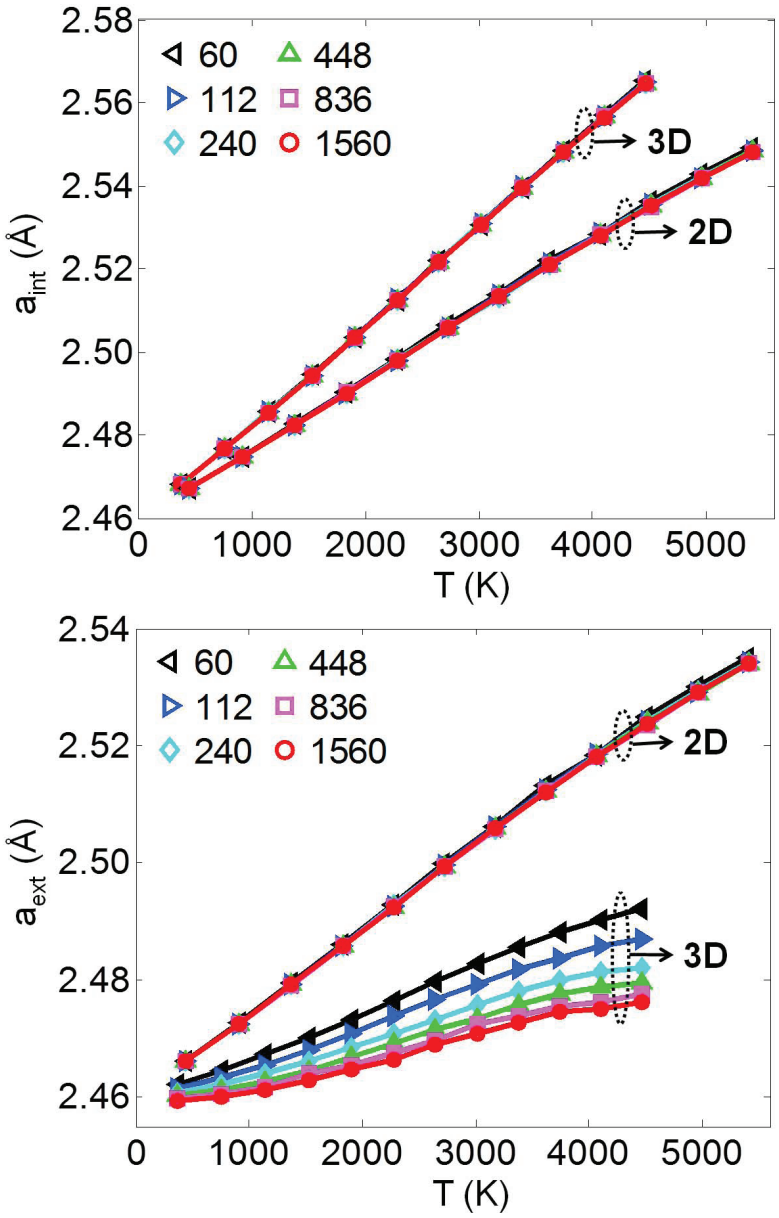

Figure 2.5: The top panel displays the internal lattice parameter $a_{\text{int}} = \sqrt{3}\langle b \rangle$ where $\langle b \rangle$ is the average bond length. The bottom panel shows the external lattice parameter $a_{\text{ext}} = L/N$ where L is the total length of the four edges of the simulation box and N is the number of primitive cells along these edges.

for case 3D). Moreover, G_T is almost identical to G_S within numerical errors, as it should be according to Landau and Lifshitz [28].

Fig. 2.7 shows adiabatic and isothermal Poisson's ratios, both of which assume positive values in the examined temperature range. Again, we recognize the already familiar size dependence pattern, *i.e.*, obvious size dependence for case 3D and nearly no size dependence for case 2D, which is compatible with Fig. 2.6 about elastic moduli. Notice that the Poisson's ratio continuously drops down, say, at room temperature as the system dimension decreases. It is possible that the Poisson's ratio of a large enough free–standing graphene film may reach a negative value.

To test the elastic isotropy of graphene at finite temperatures, define $\xi = (s_{1111} - s_{1122})/(2s_{1212})$. Note that while $\xi = 2(1+\nu)G/Y = 1$ for elastic isotropic materials, large values of ξ usually suggests highly anisotropic elastic constants. In the top panel of Fig. 2.8, $\xi \equiv 1$ for all system sizes and temperatures in case 2D. Nevertheless, ξ tends to increase with the temperature and the system size in case 3D since thermal rippling destroys the symmetry of the graphene lattice and large systems plus high temperatures often result in large out–of–plane crumpling (see Fig. 2.3). It is known that for 2D anisotropic materials, the Young's modulus or the Poisson's ratio is generally not a single constant. Therefore, Y defined in Eq. 2.8 and ν defined in Eq. 2.10 should be understood in an average sense in case 3D.

To gain further insights into the anisotropic elasticity, the bending rigidity κ are plotted against the mean local mean curvature H in the bottom panel of Fig. 2.8. Notice that the bending energy per unit area can be written as $\kappa H^2/2$ [28]. As the plot suggests, the short wavelength components of the thermal ripples traveling in different directions may have different bending rigidities. Recall that the elastic moduli of a spontaneously wrinkled graphene sheet largely depend on how difficult to unfold the thermal ripples with applied test stresses, so the elastic responses to test stresses are also generally direction dependent, which implies an anisotropic elastic behavior. Although all the graphene samples concerned here are nearly square, it turns out that the shape of the simulation box also causes anisotropy. For a concrete example, consider a rectangular system of size $L_1 = 12.78$ Å and $L_2 = 12.30$ Å which has $Y_1 \approx Y_2 \sim 19$ eV/Å^2 at $T \sim 370$ K (where Y_i are measured along the edge L_i, $i = 1, 2$). However, if we keep L_1 fixed and double L_2, then $Y_1 \sim 19$ eV/Å^2 but $Y_2 \sim 16$ eV/Å^2.

2.4 Conclusions

In summary, we have studied the temperature and size dependent elastic properties of graphene at zero stress and external pressure using the MC techniques with the HtN ensemble. The morphology of a graphene sheet at different temperatures is computed and the magnitude of the out–of–plane fluctuations of carbon atoms is shown to increase with the system size. The strong thermal rippling in large graphene membranes not only decreases

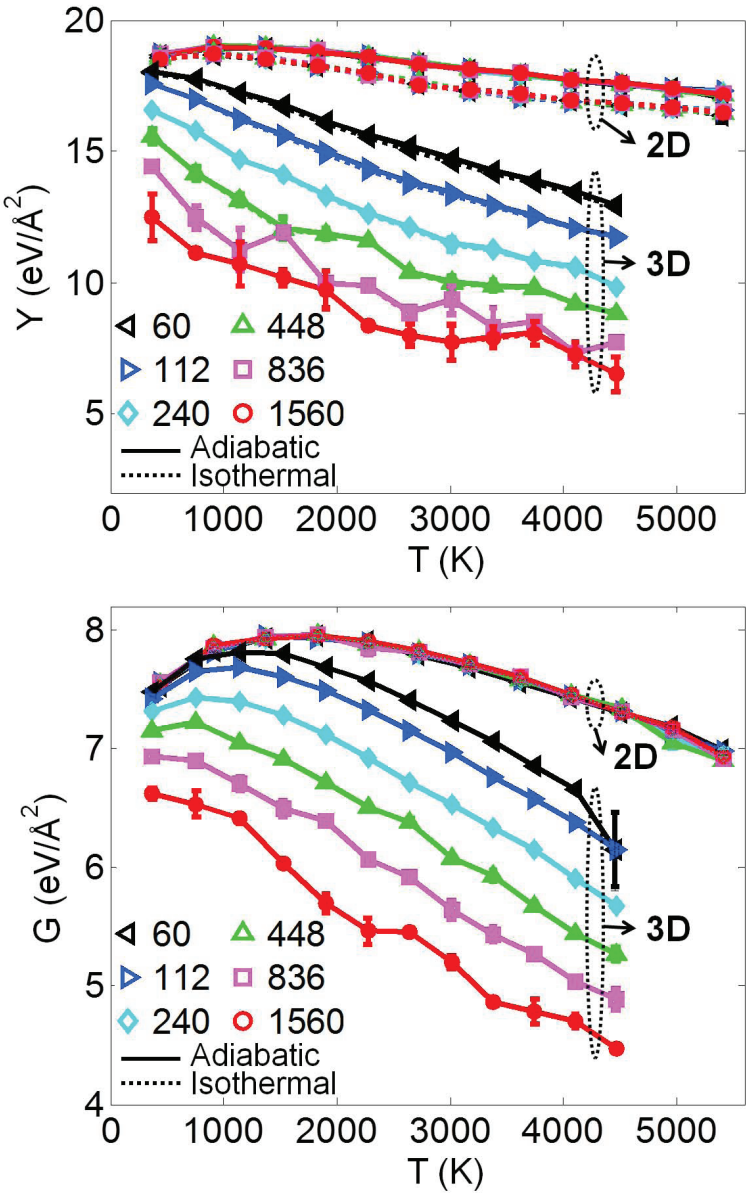

Figure 2.6: The temperature dependent and size dependent adiabatic/isothermal elastic moduli. Both the young's modulus Y (the top panel) and the shear modulus G (the bottom panel) decrease as the temperature increases. Moreover, the thermal rippling effectively brings down the moduli. The system becomes unstable (sublimation) when the temperature reaches ~ 5500 K (case 2D) or ~ 4500 K (case 3D). It is also seen that the adiabatic shear modulus is nearly the same as the isothermal shear modulus.

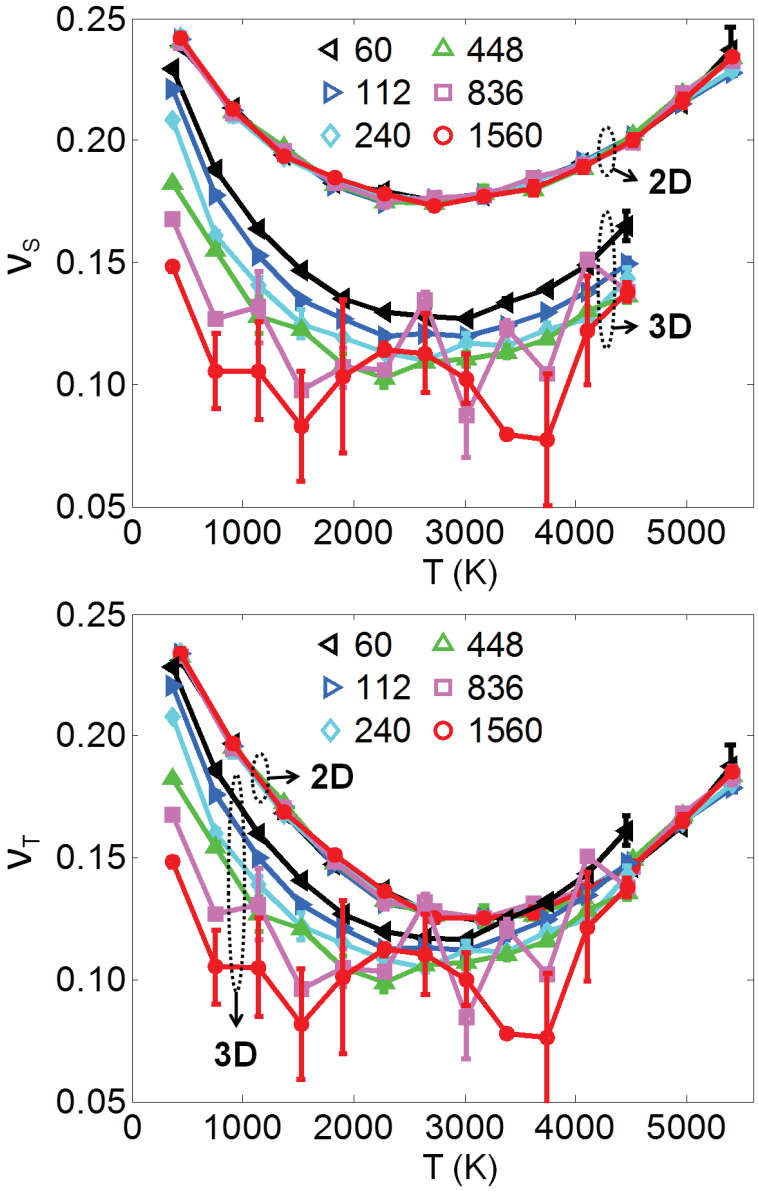

Figure 2.7: The adiabatic Poisson's ratio ν_S (the top panel) and the isothermal Poisson's ratio ν_T (the bottom panel) of several system sizes at different temperatures.

the thermal expansion coefficient and the elastic moduli, but also leads to a large deviation from the isotropic elasticity.

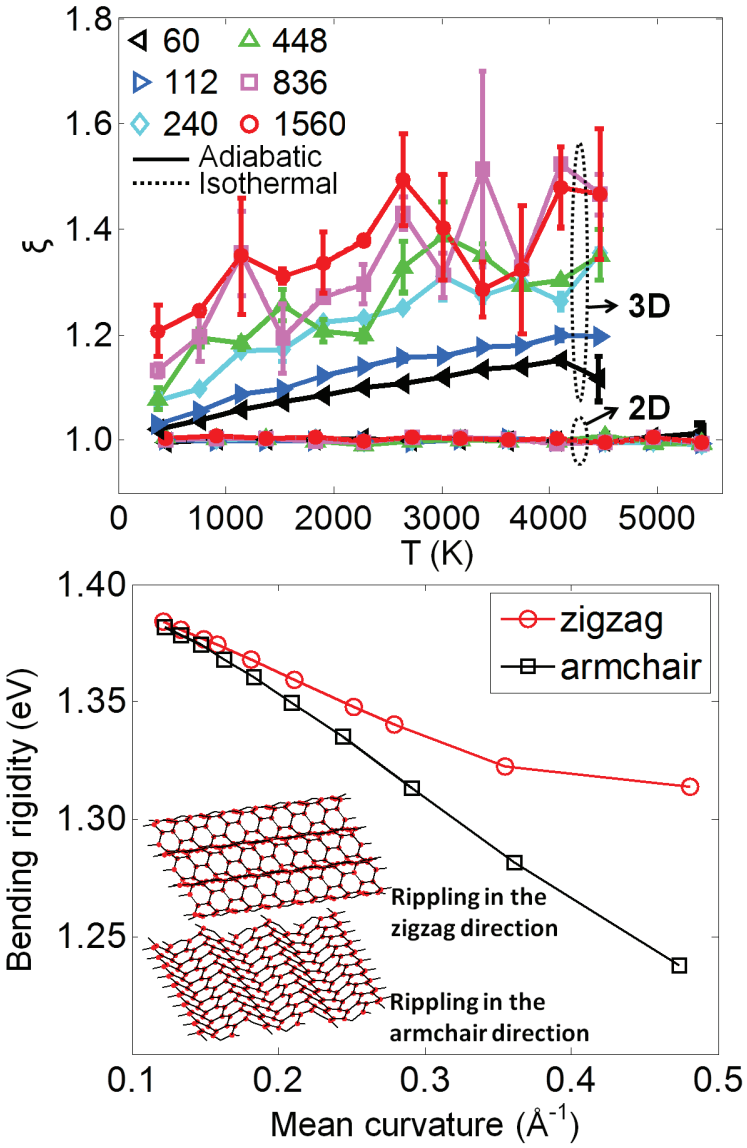

Figure 2.8: The top panel demonstrates the thermal rippling induced anisotropic elasticity quantified by $\xi = (s_{1111} - s_{1122})/(2s_{1212})$ ($\xi = 1$ for isotropic materials). Note that ξ may be calculated according to either adiabatic or isothermal elastic compliances, but the results are almost identical. The bottom panel suggests that thermal ripples propagating in different directions may have different bending rigidities.

Chapter 3

Continuum Theory of Dislocations in Graphene

3.1 Introduction

Free–standing graphene sheets and many other types of flexible membranes might be abstracted as two-dimensional manifolds embedded in a three-dimensional space. The internal strain field developed by defects such as disclinations and dislocations in these thin films can be screened effectively by nontrivial out–of–plane buckling [48]. Buckling is a critical factor in predicting defect formation energies that reflect a subtle balance between stretching and bending energies [48].

The well known Stone-Wales defect in graphene may be viewed as a tightly bounded edge dislocation dipole in a two-dimensional hexagonal lattice [12]. The formation energy and the defect core structure of a Stone-Wales defects and other dislocation dipoles have been studied extensively within many theoretical frameworks [12, 9, 23, 47, 64, 40]. This chapter is devoted to developing a continuum theory to study the interplay between buckling and dislocations in graphene (or more generally, in any flexible membrane). This interplay leads to substantial screening of the strains arising from a dislocation, and consequently yields a well-defined formation energy for a single dislocation [43, 48]. The theory enables rapid computation of the total energy of collections of defects, and thereby allows exploration of metastable buckled states.

Following Landau and Lifshitz [28], an elastic thin plate with topological defects can be characterized completely by the von Kármán equations with proper boundary conditions [48]. Instead of explicitly solving these complicated differential equations in real space [48], we assume periodic boundary conditions and directly minimize the total elastic energy of the system with respect to the strain field in Fourier space, a technique originally developed by Mura [38], later extended by Daw [6] and recently applied by Ertekin and coworkers to calculate the energy of Stone-Wales defects in flat graphene sheets and carbon nanotubes

[12, 13]. Our theory incorporates *both* the curvature contribution to the total energy and the image forces of dislocations due to periodicity, and immediately facilitates the comparison between the continuum and the atomistic methods.

3.2 Continuum Methods

3.2.1 Nonlinear Elastic Theory

In general, the bending of a flat membrane with large deflections can be described [28] by an in–plane displacement field $\mathbf{u}(\mathbf{X}) = (u_1, u_2)$ and an out–of–plane displacement function $f(\mathbf{X})$ at each point $\mathbf{X} = (x_1, x_2)$ referenced to the initial flat state in the two–dimensional space spanned by the orthogonal unit vectors $\hat{\mathbf{x}}_1$ and $\hat{\mathbf{x}}_2$. The deformation map $\mathbf{X} \to \mathbf{X}' = (x_1 + u_1, x_2 + u_2, f)$ (see Fig. 3.1a) introduces the *total strain* $u_{ij} = \varepsilon_{ij} + F_{ij}$ which is a sum of the *distortion strain* $\varepsilon_{ij} = (\Delta_{ij} + \Delta_{ji})/2$ with $\Delta_{ij} = \partial_i u_j$ and the *bending strain* $F_{ij} = \partial_i f \partial_j f/2$. Notice that in accordance with the assumption of large deflections, the nonlinear term F_{ij} must be included in the total strain [28]. As illustrated in Fig. 3.1b, the bending strain can be significant even when the total strain vanishes. The stretching energy E_s and the bending energy E_b of the membrane can be written as [48] (here and thereafter the summation rule is assumed and each index $\in \{1, 2\}$)

$$E_s = \frac{1}{2} \int \mathrm{d}^2 X c_{ijkl} u_{ij} u_{kl} \tag{3.1}$$

$$E_b = \int \mathrm{d}^2 X (\frac{1}{2} \kappa H^2 + \kappa_G K) \tag{3.2}$$

where c_{ijkl} is the elastic constant, κ and κ_G are the rigidities for the mean curvature H and the Gaussian curvature K, respectively. The total elastic energy $E_t = E_s + E_b$. When $|\nabla f| \ll 1$, we have the following approximations [48]

$$H = \nabla \cdot \left(\frac{\nabla f}{\sqrt{1 + |\nabla f|^2}} \right) \approx \nabla^2 f \tag{3.3}$$

$$K = \frac{\det(\partial_i \partial_j f)}{(1 + |\nabla f|^2)^2} \approx \det(\partial_i \partial_j f). \tag{3.4}$$

Imposing periodic boundary conditions makes κ_G a irrelevant parameter. Indeed, as shown in Fig. 3.2 a two–dimensional manifold with periodic boundaries is topologically equivalent to a 2-torus whose Euler characteristic χ is exactly zero. According to the Gauss-Bonnet theorem [35], the total Gaussian curvature of the membrane $\int \mathrm{d}^2 X K = 2\pi\chi$ therefore vanishes and we are left with

$$E_b = \frac{1}{2} \kappa \int \mathrm{d}^2 X H^2 \approx \frac{1}{2} \kappa \int \mathrm{d}^2 X (\partial_i \partial_i f)^2. \tag{3.5}$$

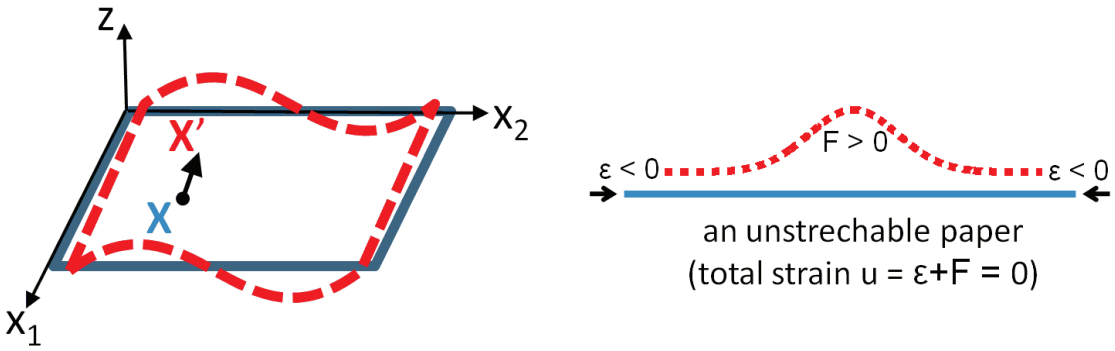

Figure 3.1: A sketch of the deformation map from a flat membrane to a buckled one (left) and an example of the bending strain for an unstretchable paper (right).

The periodic boundary conditions also permit the Fourier expansion of the stretching and the bending energies [48, 6],

$$E_s = \frac{A}{2}\sum_{\mathbf{G}} c_{ijkl}(\tilde{\Delta}_{ij}(\mathbf{G}) + \tilde{F}_{ij}(\mathbf{G}))(\tilde{\Delta}_{kl}(-\mathbf{G}) + \tilde{F}_{kl}(-\mathbf{G})) \tag{3.6}$$

$$E_b \approx \frac{A\kappa}{2}\sum_{\mathbf{G}}\sum_{i,j}(G_i^2 G_j^2)|\tilde{f}(\mathbf{G})|^2 \tag{3.7}$$

with A the area of the membrane in the flat reference state, $\tilde{\Delta}(\mathbf{G})$, $\tilde{f}(\mathbf{G})$ and $\tilde{F}_{ij}(\mathbf{G})$ the Fourier transforms of $\Delta(\mathbf{X})$, $f(\mathbf{X})$ and $F_{ij}(\mathbf{X})$ respectively, c_{ijkl} the elastic constants and κ the bending rigidity for the mean curvature H. The approximation in Eq. (3.7) is $H \approx \nabla^2 f$, valid when $|\nabla f| \ll 1$. Also note that $\tilde{F}_{ij}(\mathbf{G})$ depends on $\tilde{f}(\mathbf{G})$ explicitly.

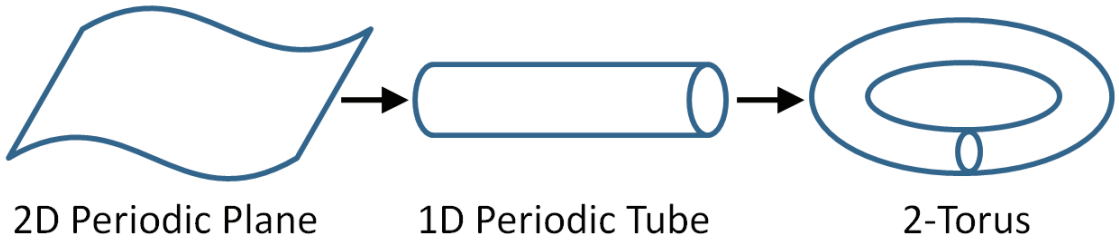

Figure 3.2: A continuous deformation (homeomorphism) between a periodic plane and a 2-torus.

The existence of N dislocations forces the topological constraints [48]

$$\alpha_k = \epsilon_{ij}\partial_i \Delta_{jk} = \sum_{\beta=1}^{N} b_k^\beta \delta(\mathbf{X} - \mathbf{X}^\beta) \tag{3.8}$$

where $\mathbf{b}^\beta$ is the burgers vector of the dislocation β at $\mathbf{X}^\beta$, α_k is the two-dimensional Nye dislocation density tensor [38], ϵ_{ij} is the permutation tensor and $\delta(\cdot)$ is the Dirac delta function. Rewriting Eq. (3.8) in Fourier space yields

$$\mathrm{i}A\epsilon_{ij}G_i\tilde{\Delta}_{jk} = \sum_{\beta=1}^{N} b_k^\beta \exp(-\mathrm{i}\mathbf{G}\cdot\mathbf{X}^\beta). \tag{3.9}$$

The solution to Eq. (3.9) consists of inhomogeneous and homogeneous parts [6], *i.e.* $\tilde{\Delta} = \tilde{\Delta}^{\mathrm{inh}} + \tilde{\Delta}^{\mathrm{hom}}$ with

$$\tilde{\Delta}_{jk}^{\mathrm{inh}} = \frac{\mathrm{i}}{AG^2}\sum_{\beta=1}^{N}(\mathbf{G}\times\hat{\mathbf{z}})_j b_k^\beta \exp(-\mathrm{i}\mathbf{G}\cdot\mathbf{X}^\beta) \tag{3.10}$$

$$\tilde{\Delta}_{jk}^{\mathrm{hom}} = -\mathrm{i}G_j\tilde{\chi}_k. \tag{3.11}$$

Here $\hat{\mathbf{z}} = \hat{\mathbf{x}}_1 \times \hat{\mathbf{x}}_2$ is the dislocation line vector. The free parameter $\tilde{\chi}_k$ can be determined by substituting Eq. (3.10) and (3.11) into Eq. (3.6) and then minimizing the total elastic energy with respect to $\{\tilde{\chi}_k(\mathbf{G})\}$, which leads to

$$c_{ijkl}G_iG_k\tilde{\chi}_j = -\mathrm{i}c_{ijkl}(\tilde{\Delta}_{ij}^{\mathrm{inh}} + \tilde{F}_{ij})G_k. \tag{3.12}$$

This is a 2×2 linear equation for $(\tilde{\chi}_1, \tilde{\chi}_2)$ and can be solved easily.

At this moment, E_t is readily written as a function of $\{\tilde{f}(\mathbf{G})\}$ only and it is a straightforward exercise to explicitly derive an analytical expression for $\partial E_t/\partial\tilde{f}(\mathbf{G})$. Next, a nonlinear programming algorithm [50, 49] is then employed to numerically find the local optimal solution of the bending modes $\{\tilde{f}(\mathbf{G})\}$ and the corresponding total elastic energy E_t. Finally, Eqs. (3.10), (3.11) and (3.12) are applied to obtain the distortion $\tilde{\Delta}_{ij}(\mathbf{G})$ and Eqs. (3.6) and (3.7) are invoked to find the stretching energy E_s and the bending energy E_b, respectively.

One way to ensure the absolute convergence of the Fourier summuation in Eq. (3.6) is to smear the singularity of $\mathbf{u}(\mathbf{X})$ by replacing the delta function in Eq. (3.8) with a Gaussian distribution [6], *i.e.*

$$\delta(\mathbf{X} - \mathbf{X}^\beta) \to \frac{1}{\pi r_c^2}\exp\left(-\frac{(\mathbf{X}-\mathbf{X}^\beta)^2}{r_c^2}\right) \tag{3.13}$$

where r_c is the dislocation core radius. In the Fourier space, the smearing requires that [6] the term $\exp(-i\mathbf{G}\cdot\mathbf{X}^\beta)$ on the right hand side of both Eq. (3.9) and Eq. (3.10) be multiplied

by the factor $\exp(-G^2 r_c^2/4)$. We further assume that the function $f(\mathbf{X})$ is smooth enough such that the Fourier summation in Eq. (3.7) is also absolutely convergent.

It is worthwhile to point out that given Eq. (3.1), (3.2) and (3.8), the variation of E_t in the real space with respect to $\mathbf{u}(\mathbf{X})$ and $f(\mathbf{X})$ leads to a modified version of the von Kármán equations [48], a set of coupled nonlinear second-order partial differential equations which are generally very difficult to solve.

3.2.2 A Working Example

The most important input parameters for the continuum model include c_{ijkl}, κ and r_c. Given an *ab initio* or classical potential, c_{ijkl} at 0 K may be obtained through the second-order derivatives of the potential with respect to strains, and κ at 0 K can be conveniently determined by fitting the equation $E_b = \kappa\pi L/r$ where E_b is the bending energy of a tube with length L and radius r. It is even possible to calculate c_{ijkl} and κ at finite temperatures using Monte Carlo simulations and fluctuation formulas [15, 32]. In order to tune and benchmark the continuum model for graphene, we employ the classical REBO potential [4] and compute the Young's modulus $Y = 16.93$ eV/Å^2, the shear modulus $G = 6.90$ eV/Å^2 and the bending rigidity $\kappa = 1.38$ eV, all at 0 K. Since graphene is an elastically isotropic material, the c_{ijkl} tensor depends on Y and G only. The dislocation core radius r_c is chosen to be 0.94 Å, an empirical value that appears to be reasonable in many cases. At finite temperatures, we may employ the MC techniques with the HtN ensemble [15] as described in chapter 2 to determine the elastic constants (in case 2D).

In Fig. 3.3, the continuum model is employed to calculate the strain field of a pair of dislocations separated by $6a$ where $a = 2.46$ Å is the lattice parameter for the hexagonal lattice of a flat graphene sheet. Notice that periodic boundary conditions are imposed. Evident out-of-plane crumpling around 3 Å is observed. Moreover, the curl of the strain field is nonzero around each dislocation, in accordance with Eq. 3.8. Once the total strain field is known, the displacement field may be obtained by integration along, say, paths that do not intersect the defined displacement cut. As expected, the computed displacement has a jump across the cut.

3.3 Results and Discussions

3.3.1 Continuum Model *vs.* Atomistic Model

Consider the elementary case of a single dislocation dipole with one dislocation fixed and the other gliding. The continuum model is employed to calculate $\{\tilde{f}(\mathbf{G})\}$ from which the real space membrane surface $f(\mathbf{X})$ is constructed. Afterwards, in the atomistic model the corresponding defected sheet of atoms are bent according to $f(\mathbf{X})$ and then relaxed using the conjugate gradient method with periodic boundary conditions. In Fig. 3.4, we explore

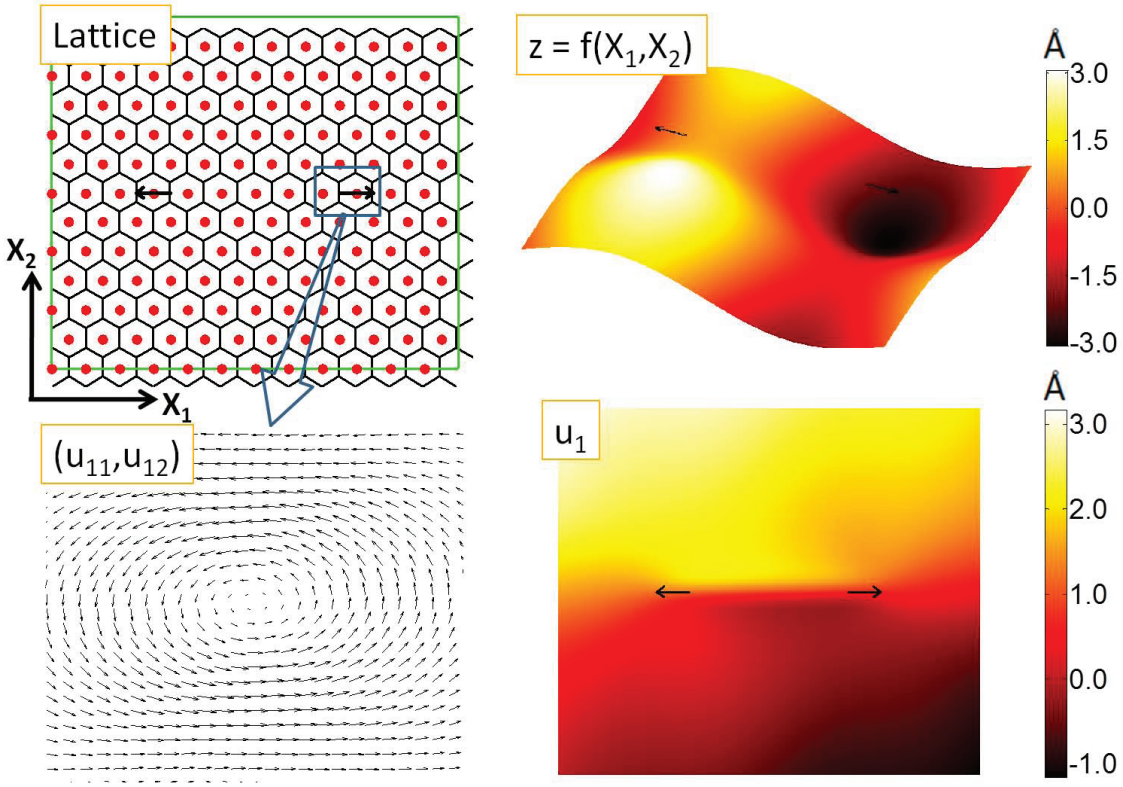

Figure 3.3: The total/bending strain field computed by the continuum model for a graphene membrane with a dislocation dipole. The top left panel sketches the 2D hexagonal lattice for graphene and labels the dislocation positions and the Burgers vectors (the two small arrows). The top right panel displays the defect induced out-of-plane buckling. The bottom left panel illustrates the total strain field around one dislocation. The bottom right panel shows the displacement field in the horizontal direction.

such an example for a 59.18 Å × 51.25 Å graphene sheet with 1152 atoms. Starting from a Stone-Wales defect at step 1, the moving dislocation glides by one lattice parameter (2.46 Å) along its slip plane at each of the following steps. Notice that when buckling is forbidden, one recovers linear elastic theory [6, 12].

Let E_t and $E_t^{\rm A}$ be the total elastic energies computed from the continuum theory and the REBO potential respectively. As shown in the top panel of Fig. 3.4, for both flat and buckled sheets, E_t and $E_t^{\rm A}$ match quite well at all steps except the initial one. If we define the relative error δ to be $\Delta E/E_t^{\rm A}$ where $\Delta E = E_t - E_t^{\rm A}$, then for the flat sheet, at step 1, $\delta_1 = -10.19\%$, while for the remaining steps, the average error $\bar{\delta}$ is only $-0.28\% \pm 0.54\%$; for the buckled sheet, $\delta_1 = -8.63\%$ and $\bar{\delta} = 3.20\% \pm 0.72\%$. The fact that the latter $|\bar{\delta}|$ is bigger may be attributed to the approximation in Eq. (3.7) which is no longer good in regions with significant bending. For example, in the bottom panel of Fig. 3.4, when $\mathbf{X}$ is in the vicinity of a dislocation, $|\nabla f(\mathbf{X})|$ reaches its maximum value ~ 0.62, a value that makes the assumption $|\nabla f(\mathbf{X})| \ll 1$ questionable. It is recognized that the continuum model tends to underestimate the total energy for a Stone-Wales defect ($\delta_1 < 0$) and results in systematic large errors ($|\delta_1| > |\bar{\delta}|$). The two dislocations within a Stone-Wales defect are very near to each other and this short ranged interaction between dislocations is not described well by the current theory.

However, it is surprising to see that the continuum theory works for such small systems as in Fig. 3.4. In fact, we have examined even smaller system of 29.59 Å × 25.63 Å with 288 atoms and the continuum theory still matches well with the REBO potential. Furthermore, the continuum method can deal with more complex dislocation patterns other than a single dipole. We have studied a dislocation quadrupole where one pair of dislocations is stationary and the other pair moves together which first glides and then climbs (Fig. 3.5). Again, the continuum theory not only identifies important bending modes of the membrane but also nicely captures the trend of the total energy change. It should be clear that in this example, the total mass is still conserved because two dislocations with opposite signs climb *simultaneously*. One drawback of our present theory is that only the conservative movements of dislocations are incorporated. Various types of nonconservative movements such as the climb of a single dislocation inevitably introduces vacancies and are not discussed here. Nevertheless, it is very interesting to understand the interactions between vacancies and dislocations in *buckled* membranes, which deserves further investigations in the future.

As we have emphasized before, buckling has an important impact on the total elastic energy. To illustrate this point, denote $\hat{E}$ as energy per area and expand Eq. (3.6) as $\hat{E}_s = \hat{E}_s^{\Delta} + \hat{E}_s^{F} + \hat{E}_s^{\Delta F}$ where $\hat{E}_s^{\Delta}$, $\hat{E}_s^{F}$ and $\hat{E}_s^{\Delta F}$ are energies due to $\tilde{\Delta}$, $\tilde{F}$ and the interaction term $\tilde{\Delta}\tilde{F}$, respectively. Focusing on the bottom panel of Fig. 3.4, although the free membrane has a fixed zero total strain, its sine–like shape implies a nonzero bending strain $F_{11} = 3.58\%$, $F_{22} = 0.95\%$ and $F_{12} = 0$ associated with a positive bending energy. However, at the same time the stretching energy is greatly reduced because of the interaction term $\hat{E}_s^{\Delta F}$. More specifically, for the flat sheet $\hat{E}_t = \hat{E}_s = \hat{E}_s^{\Delta} = 6.71$ meV/Å^2, while for the buckled sheet $\hat{E}_s^{\Delta} = 31.74$ meV/Å^2, $\hat{E}_s^{F} = 28.10$ meV/Å^2, $\hat{E}_s^{\Delta F} = -57.93$ meV/Å^2, $\hat{E}_b = 1.72$ meV/Å^2

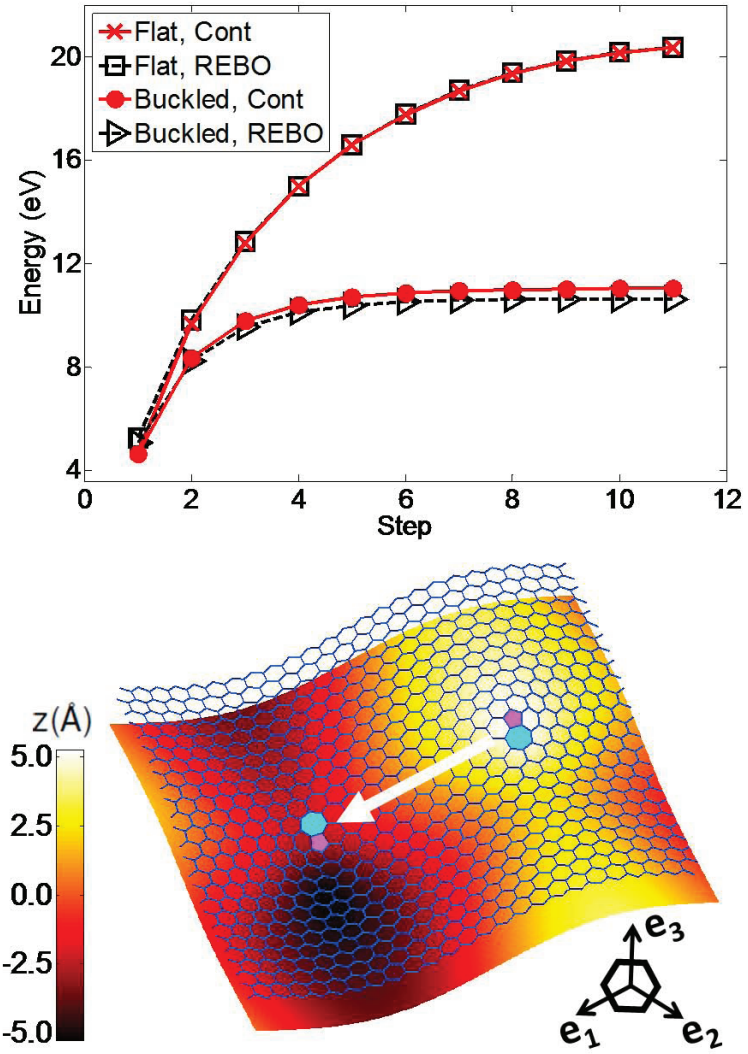

Figure 3.4: A comparison between the continuum model and the atomistic model (REBO) in the case of a dislocation dipole. The top panel shows the dislocation dipole energies calculated through the continuum method and the REBO potential in a graphene membrane that is either forced to be flat or is allowed to buckle. At each step, one dislocation is stationary and the other one is moving along the slip plane $\mathbf{e}_1$. The bottom panel presents the buckled membrane surface at the last step as well as the corresponding optimized atom configuration where a pair of neighboring pentagon and heptagon stands for a two-dimensional edge dislocation.

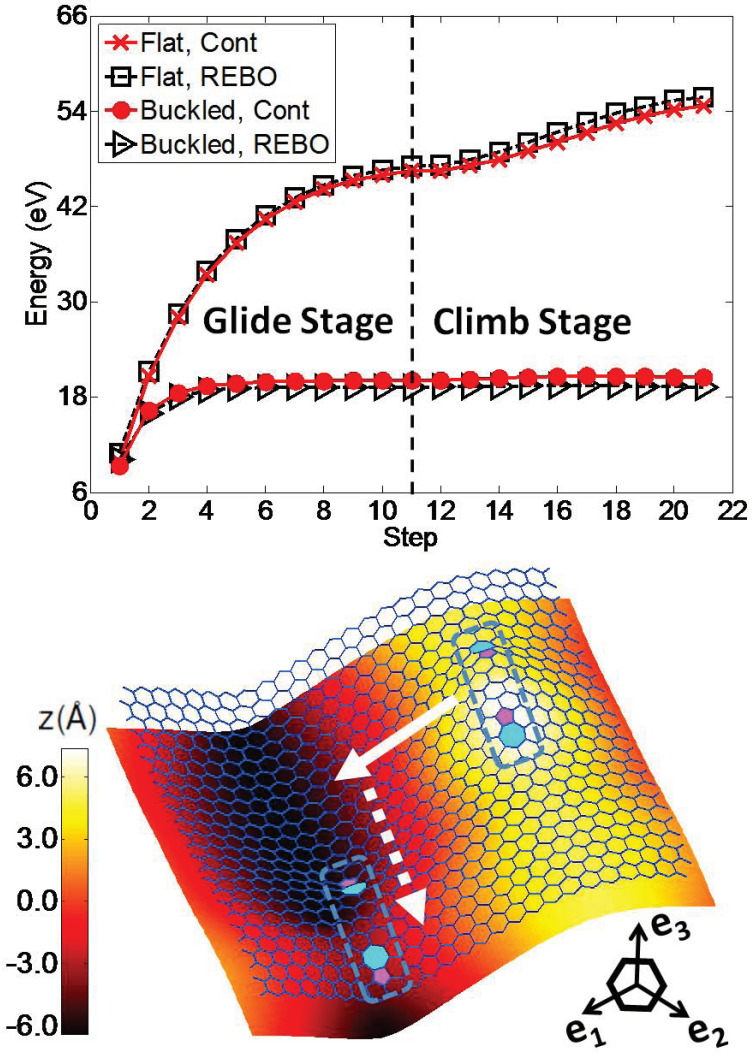

Figure 3.5: A comparison between the continuum model and the atomistic model (REBO) in the case of a dislocation quadrupole. The top panel shows the dislocation quadrupole energies calculated through the continuum method and the REBO potential in a graphene membrane that is either forced to be flat or is allowed to buckle. At each step, one dislocation dipole is stationary and the other one is moving along the slip plane $\mathbf{e}_1$ and then climbs together. The bottom panel presents the buckled membrane surface at the last step as well as the corresponding optimized atom configuration.

and thus $\hat{E}_s = 1.92$ meV/Å^2, $\hat{E}_t = 3.64$ meV/Å^2. Now, it is obvious that $\hat{E}_s^{\Delta F}$ is the only term that actually decreases E_s and E_t.

3.3.2 Finite Dislocation Energy

As we have seen in Fig. 3.4, the dipole formation energy E_t is reduced due to buckling. In addition, it appears that the energy approaches a constant as the distance r between the two dislocations increases. Plotting E_t as a function of r/b for large systems (Fig. 3.6) where $b = 2.46$ Å is the Burgers vector, the trends clearly suggest that for flat graphenes the formation energy of a single dislocation $E_d(r) = E_t(r)/2$ follows $E_d(r) \sim \log(r)$, whereas for buckled graphenes, $E_d(r) \sim 12.33/2 = 6.17$ eV when r is big. The results are in good agreement with the earlier argument that the energy of a buckled dislocation is finite in an infinite large system [43, 48]. Indeed, according to Seung and Nelson [48], the buckling radius $r_b \sim 127\kappa/(Yb) = 4.21$ Å and thus $E_d(\infty) \sim (8\pi)^{-1} Yb^2 \log(r_b/r_c) \sim 6.11$ eV which is close to our value 6.17 eV.

Recall that in the theory of two–dimensional melting [17], a flexible membrane will melt into a hexatic phase at any finite temperature in the thermodynamic limit due to the fact that a finite $E_d(\infty)$ is eventually dominated by the entropy term [48] $\sim 2k_B \log(r/r_c)$. In other words, an infinite graphene sheet *cannot* maintain its crystalline structure because the long–range translational order is destroyed by the simultaneous dissociation of dislocation pairs [17].

However, in practice, graphene is a well defined two–dimensional crystal at least at room temperature. The reason for that is the extremely high value of $E_d(\infty)$. As a crude estimate [17], a sheet with size r will melt when $E_d(\infty) \sim 2k_B T \log(r/r_c)$. Therefore, for a melting temperature $T_m = 300$ K, $r \sim r_c \exp(E_d(\infty)/(2k_B T_m)) \sim 10^{41}$ m which is much greater than the diameter of the observable universe ($\sim 10^{27}$ m)! Nevertheless, $T_m = 4000$ K corresponds to a much smaller and reasonable $r \sim 700$ nm for a real experiment.

3.3.3 Applications

The continuum theory can be extended to handle other interesting situations. For instance, i) suppressing the buckling at the boundaries is equivalent to a group of *linear* constraints: $\sum_{G_1} \tilde{f}(\mathbf{G}) = 0$ for any G_2 and $\sum_{G_2} \tilde{f}(\mathbf{G}) = 0$ for any G_1; ii) applying an external in–plane stress field $\sigma_{ij}(\mathbf{X})$ and a pressure $p(\mathbf{X})$ normal to the membrane can be modeled by adding a work term $-A \sum_{\mathbf{G}} (\tilde{\sigma}_{ij}(\mathbf{G}) \tilde{\Delta}_{ij}(-\mathbf{G}) + \tilde{p}(\mathbf{G}) \tilde{f}(-\mathbf{G}))$ to E_s where $\tilde{\sigma}_{ij}(\mathbf{G})$ and $\tilde{p}(\mathbf{G})$ are the Fourier transform of $\sigma_{ij}(\mathbf{X})$ and $p(\mathbf{X})$ respectively.

The controlled rippling of graphene recently realized in experiments [1] can be modeled using the continuum theory. As illustrated in Fig. 3.7), a graphene ribbon of $L_x = 118.36$ Å and $L_y = 25.63$ Å with buckling suppressed at its edges along the x–direction is subjected to an in–plane compressing stress $\sigma_{xx} = -0.2$ eV/Å^2. Such boundary conditions lead to periodic wrinkles with a wavelength $\lambda \sim L_x/4 = 29.59$ Å which matches very well with a

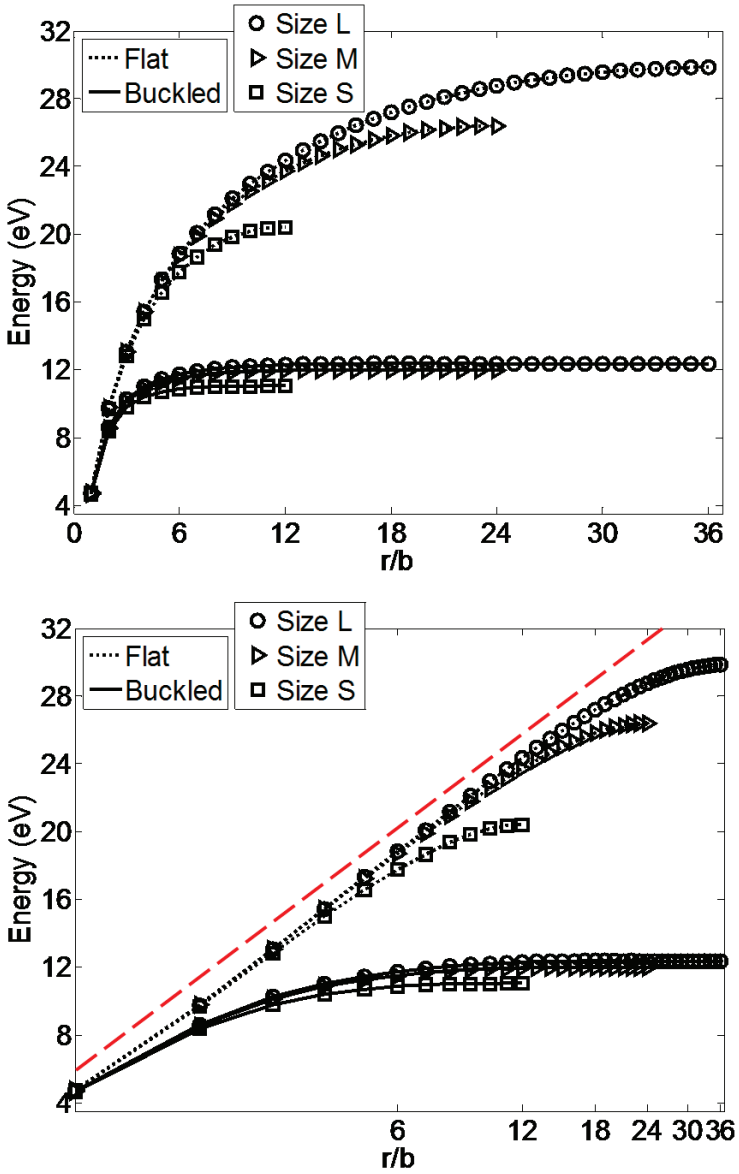

Figure 3.6: The dipole formation energy E_t as a function of distance r between the two dislocations consisting of the dipole. The x–axis r/b where b = 2.46 Å is set either in the regular scale (the top panel) or in the logarithmic scale (the bottom panel). The graphene sheet could be flat or buckled. The dipole orientation is similar to that in Fig. 3.4. Three system sizes are considered, namely, size S is 59.18 Å × 51.25 Å, size M is 118.36 Å × 102.51 Å and size L is 177.55 Å × 153.76 Å.

general theory of wrinkling [5] that estimates $\lambda \sim 2\sqrt{\pi L_y}(\kappa/\sigma_{xx})^{1/4} = 29.08$ Å. The angle of the wrinkles can also be adjusted by applying a shear stress [60]. As shown in the bottom panel of Fig. 3.7, the addition of a shear of 0.1 eV/Å^2 tilts the wrinkles by $\sim 57\,^\circ$.

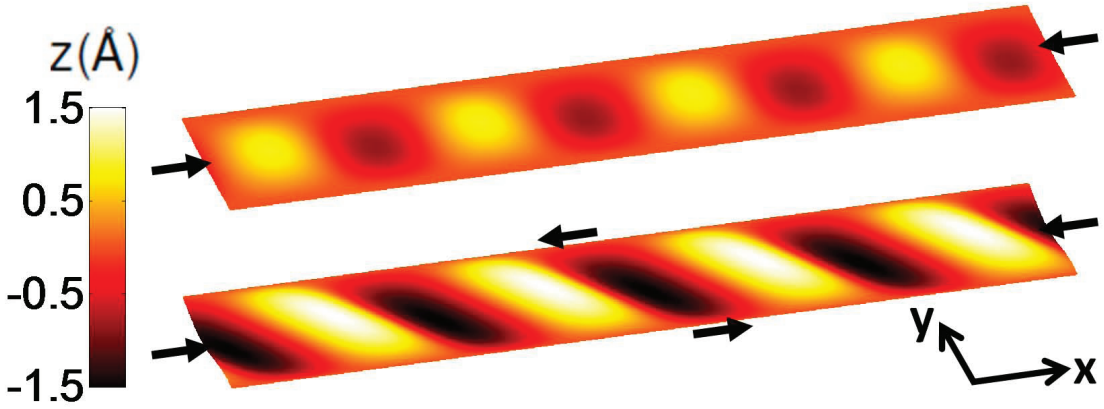

Figure 3.7: The shear stress controlled wrinkling of graphene. Edges in the x–direction are constrained to have no buckling. A compressing stress produces periodic wrinkles (the top panel) which could be slanted by the addition of a shear stress (the bottom panel).

It is a familiar fact that an in–plane pulling or shearing stress encourages plastic deformations and the nucleation of corresponding dislocations. However, carefully designed normal loadings may also effectively decrease the defect formation energy. Fig. 3.8a and 3.8b demonstrate the creation of a pair of dislocations separated by $6b$ in a 44.39 Å $\times$ 25.63 Å membrane with edges that are constrained to have no buckling. The loading P follows a Gaussian distribution with $P_{\max} = 1.00$ eV/Å^3 = 0.16 TPa and a standard deviation 1.0 Å, which is a simple model for the force field of a probe–like nanoindenter. Removing the loadings results in a mechanically stable defected sheet (Fig. 3.8c) with a total elastic energy 12.77 eV. In comparison, the dipole nucleated in the loaded membrane (Fig. 3.8a) has a much lower formation energy, only 1.17 eV. It is also found that there is a mechanically metastable state as shown in Fig. 3.8e. The elastic energy of this state is 12.94 eV. By pressing down (*e.g.* Fig. 3.8d) or pulling up the bubble around a dislocation, it is possible to go back and forth from the stable state to the metastable state.

The loadings in Figs. 3.8a and 3.8b might be realized using two scanning probes. Experimentally, it is probably more simple to apply a single probe. Even in this case, the probe can be used to reduce the defect formation energy, though the reduction is much reduced in comparison to the two probe case. Figure 3.9 shows deformation under a single probe before and after the introduction of a dislocation dipole. In this case, E_t is reduced from 12.77 eV to 7.93 eV.

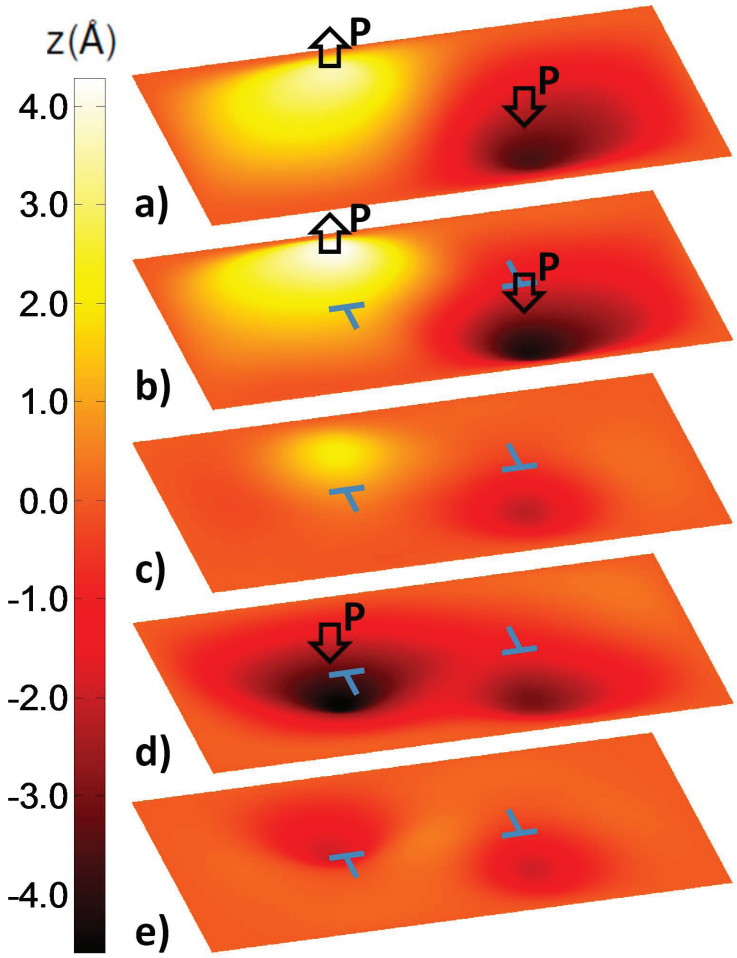

Figure 3.8: Modeling nanoindentation of a defected graphene sheet with buckling suppressed at all boundaries. External normal loadings produce a buckled surface (panel a) which facilitates the nucleation of a dislocation dipole (panel b). After the loadings are removed, the system sits in a mechanically stable state with an either upward or downward bubble around each dislocation (panel c). The upward bubble can be pressed down (panel d), leading to a metastable state where both bubbles are downward (panel e).

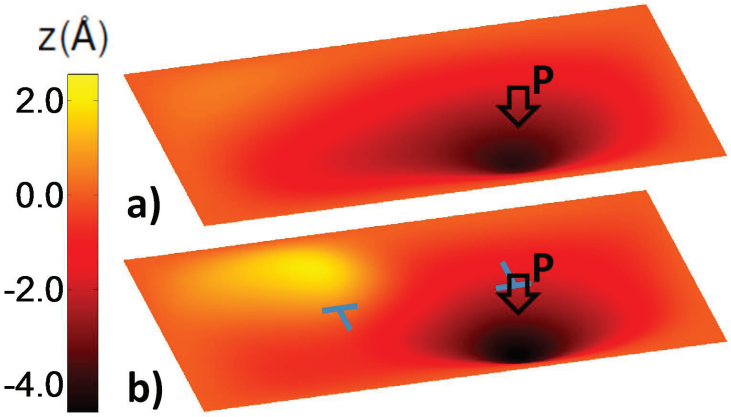

Figure 3.9: Similar scenarios as Fig. 3.8a and 3.8b except that the normal loading is exercised by a single probe.

3.4 Conclusions

In summary, a nonlinear continuum model is developed to describe dislocations in a crystalline membrane with large deflections. Under periodic boundary conditions, the topological constraints imposed by dislocations are transformed into a set of algebraic equations in Fourier space. The total energy subjected to these constraints are minimized, giving in–plane strains and out–of–plane displacements. When applied to graphene. The elastic energies and bending modes computed from the continuum theory match well with more detailed atomistic models. Furthermore, it is found that buckling effectively screens the elastic field of dislocations, which results in a well defined formation energy (~ 6.17 eV) for a single dislocation in the thermodynamic limit. Therefore, we may assume the familiar Arrhenius law to calculate the density of dislocations in a free–standing graphene. In practice, the continuum theory provides an efficient approach to simulate many interested mechanical properties of graphene sheets.

Chapter 4

Plasticity in Carbon Nanotubes

4.1 Introduction

Recent experiments into the nature of deformation and plasticity in graphene and carbon nanotubes (CNTs) suggest that the mechanical properties of two dimensional systems are complex and unique in their own right. The intrinsic strength of these carbon–based systems is predicted to exceed that of any known material [44], an expectation that is quantitatively supported by newly reported experimental measurements [44, 30]. Images of topological defects in graphene and single–walled carbon nanotubes (SWNTs) have been directly obtained via high resolution transmission electron microscopy [18, 53], indicating that defects accumulate near kinks in the plastic deformation of the tube [53]. Experimental observations of the intrinsic ripples in graphene [34], and computational explanations thereof [14] indicate that buckling and bending play an active role in the deformation. We present in this chapter theoretical and computational evidence for a novel deformation mechanism in CNTs and possibly other sp^2 carbon systems: a stress–dependent cooperative motion of dislocations that gives rise to plasticity. This deformation mechanism exists alongside more conventional dislocation glide, and arises from a complex and unique interplay between buckling, plasticity, and intrinsic defect core energies which can only occur in two–dimensional systems.

Graphene, CNTs and other sp^2 carbon systems can be thought of as two–dimensional manifolds that are free to deform (bend, stretch, buckle, *etc.*) in the three–dimensional space in which they are embedded. Plastic deformation in sp^2 carbon systems is proving to be a very interesting phenomenon. Although direct experimental investigations into the nature of the deformation of carbon membranes have only recently become accessible, the existence of defects analogous to dislocations in conventional three–dimensional materials were previously predicted and explored computationally [31, 12, 13, 8, 7, 64]. Experimental efforts [22, 21, 20, 19] have also been undertaken to elucidate how topological (*e.g.*, Stone–Wales) defects and their motion enable plastic deformation in these systems. For instance, CNTs have been shown to undergo elongations of over 280% at high temperature under

tensile loads [22]. This elongation is accompanied by a reduction in nanotube diameter and the movement of kinks along the nanotube axis, indicating a defect–mediated mechanism of plastic deformation operational at the nanoscale. Indeed, it has long been appreciated that understanding stability, deformation, and plasticity in graphene–based systems is critical for exploiting their unique properties in real world applications.

Developing theories of plasticity in CNTs and other sp^2 carbon systems is a nontrivial endeavor. The fact that one must model large volumes of material limits progress. Even more limiting, however, is the fact that plastic deformation takes place on time scales much longer than can typically be addressed within direct atomic scale molecular dynamics (MD) methods [39, 41, 54]. In this chapter, we develop a Monte Carlo sampling framework that can efficiently sample the phase space consisting of all possible C–C bond rotations in an sp^2 carbon network. Our approach discovers a novel topological defect pattern that is intrinsically different from other well documented ones, for example, vacancies [18, 29], glide [61], brittle fracture [61], sublimation of carbon dimers [7, 8], carbon ad-dimers [51], *etc.* This pattern emerges as an array of closely packed edge dislocations with alternating signs and is generally favored in tubes with large radii and under high tensile stresses. We further investigated the energetic stability of this pattern and its competing mechanisms such as dislocation glide and brittle fracture. The temperature effects on the formation of various defect patterns and the plasticity of CNTs are studied using kinetic Monte Carlo (KMC) simulations.

4.2 Simulation Methods

4.2.1 KMC Scheme

Our model relies on the following assumptions to sample the potential energy surface (PES). First, the system maintains sp^2 bonding and a constant number of atoms and bonds, *i.e.*, N carbon atoms and $3N/2$ bonds (when periodic boundary conditions are imposed). Second, generation of four sided rings and enneagons is prohibited. The topology of the system is used to characterize the states accessible from the current state by C-C bond rotations. That is, in each Monte Carlo step, a single bond rotation drives the system from the current state to the next. For instance, starting from a defect free carbon membrane, the rotation of the first bond creates a Stone-Wales defect. Subsequent rotations can annihilate the original Stone-Wales defect, create an additional Stone-Wales defect, create an octagon that leads to strain localization and brittle failure, or move an existing dislocation by one Burger's vector (Fig. 4.1). The atomic configuration of each state is optimized subject to the constraint that its bonding topology is fixed. In this way, PES local minima are sampled.

The classical REBO potential [4] is employed for most of our investigations. We are primarily interested in armchair (n, n) CNTs that are believed to be ductile at low strain and high temperature [39]. Stress relaxation and creep "experiments" are implemented by apply-

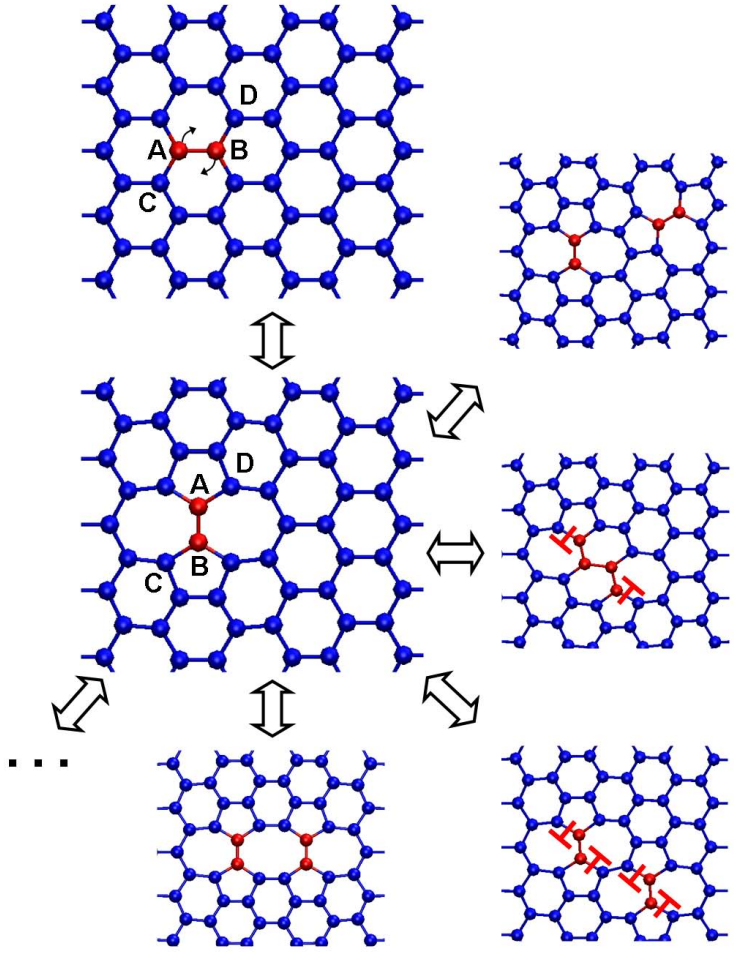

Figure 4.1: The migration of a sp^2 carbon system from one state to another by bond rotations. Each rotation involves four atoms, *e.g.*, those labeled with A, B, C, D. The topology of the system is changed by breaking two old bonds (AC and BD) and forming two new bonds (AD and BC).

ing a constant displacement per unit length or force, respectively, along the tube. Periodic boundary conditions are employed. The force normalized by the initial tube circumference is defined as the engineering stress. Geometric optimizations at each step are implemented by the fast inertial relaxation engine (FIRE) [2]. Forces are computed using analytical derivatives of the REBO potential. The root mean square force of the optimized structures is less than 10^{-4} eV/Å.

Within KMC transition rates from the current state to all eligible next states are defined to be $r_{ij} = \nu \exp(-E_{ij}^{\text{act}}/k_B T)$ where r_{ij} is the transition rate from state i to state j, E_{ij}^{act} is the corresponding energy barrier, ν is the attempt frequency, T is the temperature and k_B is the Boltzmann constant. The residence time on the current state and the choice of the next state are determined in the standard manner [3]. We consider two formulations. In the first, rates are determined entirely by initial and final state energies. The second approach incorporates explicit energy barriers, which turns out to be a tricky issue and will be discussed in detail in the next section.

A typical KMC step involves a large number of atomic scale relaxations. First, each bond is identified. The bond rotation is applied, and the atomic scale structure determined, along with the change in energy. The energy barrier is then calculated if necessary. For N atoms, the system contains $3N/2$ bonds and there are two possible rotations per bond for a total of $3N$ minimizations and saddle point identifications per KMC step. The approach is general, and can incorporate PESs computed using empirical and first principles approaches.

4.2.2 Energy Barriers

Unfortunately, PESs predicted by the classical REBO potential [4] are not smooth enough to have well defined Hessian Matrices at every point. The nonanalytic behavior frustrates saddle point identification methods. To illustrate this point, the PES of creating one Stone-Wales defect within a buckyball, C_{60}, is constructed along two chosen reaction coordinates [11] while relaxing all other degrees of freedom (Fig. 4.2a). The REBO potential leads to a PES with cusps whereever two sheets of the energy surface characterized by differing bonding topologies meet. These cusps are probably due to the bond breaking and forming during the defect nucleation and the fact that the REBO potential computes the total energy as the sum of all bond energies.

Therefore, as an alternative, we use an ad hoc pseudo reaction coordinate method to estimate energy barriers. Since each bond rotation only affects the bonding of four atoms [11], *e.g.*, atoms A, B, C, D in Fig. 4.1, we define $\mathbf{AB}\cdot\mathbf{CD}$ as a pseudo reaction coordinate, where $\mathbf{AB}$ represents a vector connecting atom A to atom B, etc. Several constrained optimizations along a path varying the reaction coordinate are executed to locate the transition state between the initial and final states. Several points between the initial and final configuration are sampled. At each point, $\mathbf{AB}\cdot\mathbf{CD}$ is fixed to some value and the total energy is obtained through a constrained structural optimization. The peak value of the energy path along the reaction coordinate is estimated by the choosing the maximum of a natural cubic spline

passing through the sampled points.

Fig. 4.2b shows an example of the energy path in the case of C_{60}. For each saddle point, we sample 10 points along the pseudo reaction coordinate. The configurations are chosen near the initial and final states. The bond in question is rotated in 0.171 radian increments for five increments from each of the endpoints. The peak value is identified at 5.0 eV using a natural spline interpolation, in comparison with 6.2 eV using an *ab initio* approach [11]. Fig. 4.2b shows a comparison between the saddle point determined in this fashion and the PES predicted by the REBO potentials.

More generally, the approach produces a reasonable description of the energy surface. In load–free (6,6), (5,5) and (4,4) tubes, the activation energy barrier of a single Stone-Wales defect is, respectively: 9.4 eV, 9.1 eV, 8.9 eV in *ab initio* [10] and 8.7 eV, 8.5 eV, 8.1 eV in our calculations; in the (5,5) tube, the activation energy of the same defect at 0.06, 0.12 and 0.15 strain is, respectively: 6.5 eV, 3.9 eV, 3.0 eV in *ab initio* [10] and 7.1 eV, 4.7 eV, 3.1 eV in our calculations. Our approach thus yields satisfactory trends.

4.3 Results and Discussions

4.3.1 Dislocation Worms

As a first step, we consider a simple relaxation model in which transition rates are determined solely by the differences between initial and final energies, and the process that is most rapid is always selected. These simulations are economical, and enable the identification of candidate deformation mechanimsms. A (10,10) CNT 47.073 Å long composed of 2760 atoms and including 4140 bonds is modeled. Periodic boundary conditions are employed. Two constant engineering stress "experiments" are carried out by initially loading the tube with a fixed engineering stress of 1.105 eV/Å^2 (initial strain of $\sim 7.8\%$) and a fixed engineering stress of 1.635 eV/Å^2 (initial strain of $\sim 13.0\%$), respectively. The results are summarized in Fig. 4.3, Fig. 4.4, Fig. 4.5 and Fig. 4.6.

At low stress, as shown in Fig. 4.3, after the initial plastic event of creating a simple edge dislocation dipole separated by three burgers vectors, subsequent deformation steps simply separate the dipole. This process is equivalent to dislocation glide in 3D. One striking difference, however, is that the motion of dislocations in CNT leads to non-negligible buckling of the tube near the dislocations (Fig. 4.4). At high stress, as shown in Fig. 4.5 and Fig. 4.6, one sees a very different deformation pattern. The initial step is, again the creation of a simple dislocation dipole. The following steps, however, are very different. Instead of the dislocation gliding as at low stress, subsequent steps lead to the formation of a chain of dislocation dipoles with no net Burgers vector. Eventually, the dipole chain breaks, yielding two edge dislocations of opposite sign, each screened by an array of dislocation dipoles. The subsequent steps either lengthen these arrays by the creation of an additional dipole immediately in front of the dislocation array or shorten them by the annihilation of the

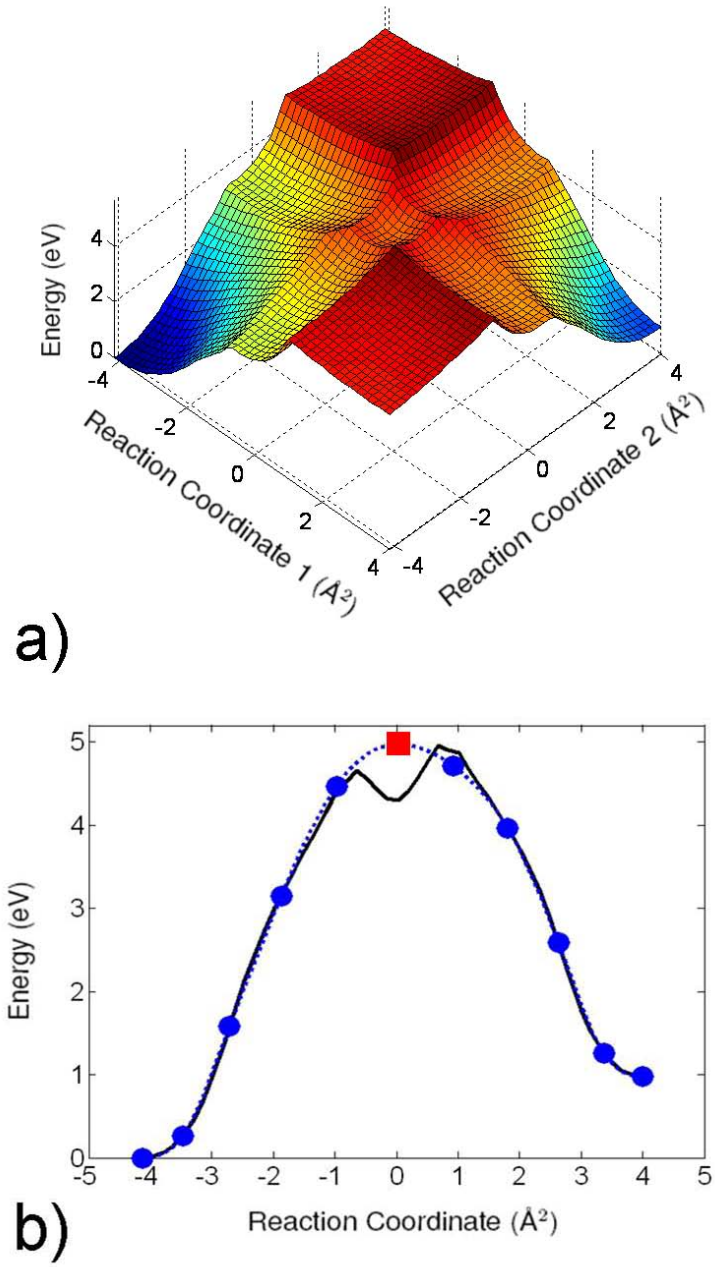

Figure 4.2: The 2D PES of creating a Stone-Wales defect in C_{60} computed by the classical REBO potential a) and the energy profile along the pseudo reaction coordinate b) where the maximum point (the red square) is identified through natural splines (the dotted blue line) based on 10 sampled points (the blue dots). For comparison, it also shows in b) the projection (the solid black line) of 2D PES in a).

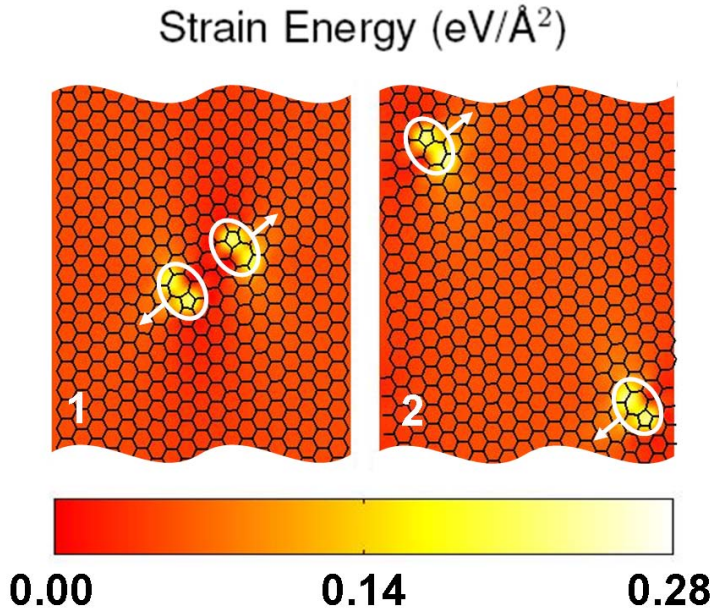

Figure 4.3: Contour plots of strain energy in (10,10) CNTs under low axial stress (1.105 eV/Å^2). The dislocations are labeled by circles with arrows indicating the glide direction.

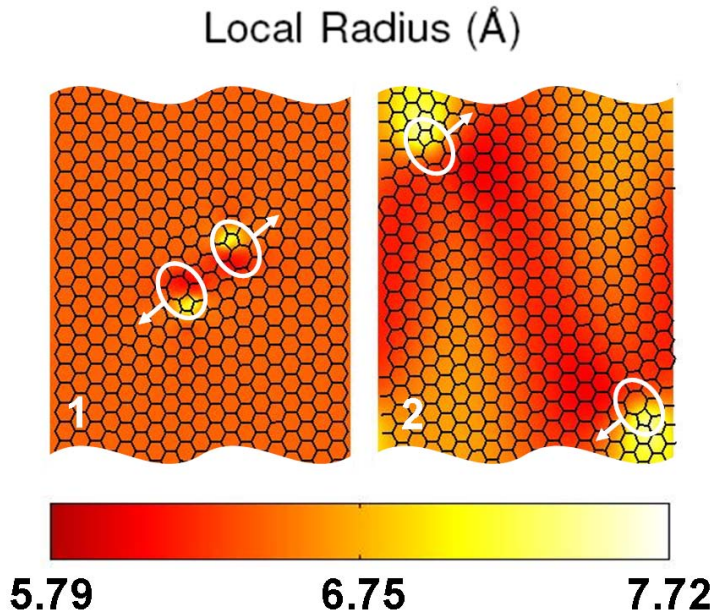

Figure 4.4: Contour plots of local tube radius correspond to Fig. 4.3. It is observed that carbon membranes are significantly buckled around the two gliding dislocations.

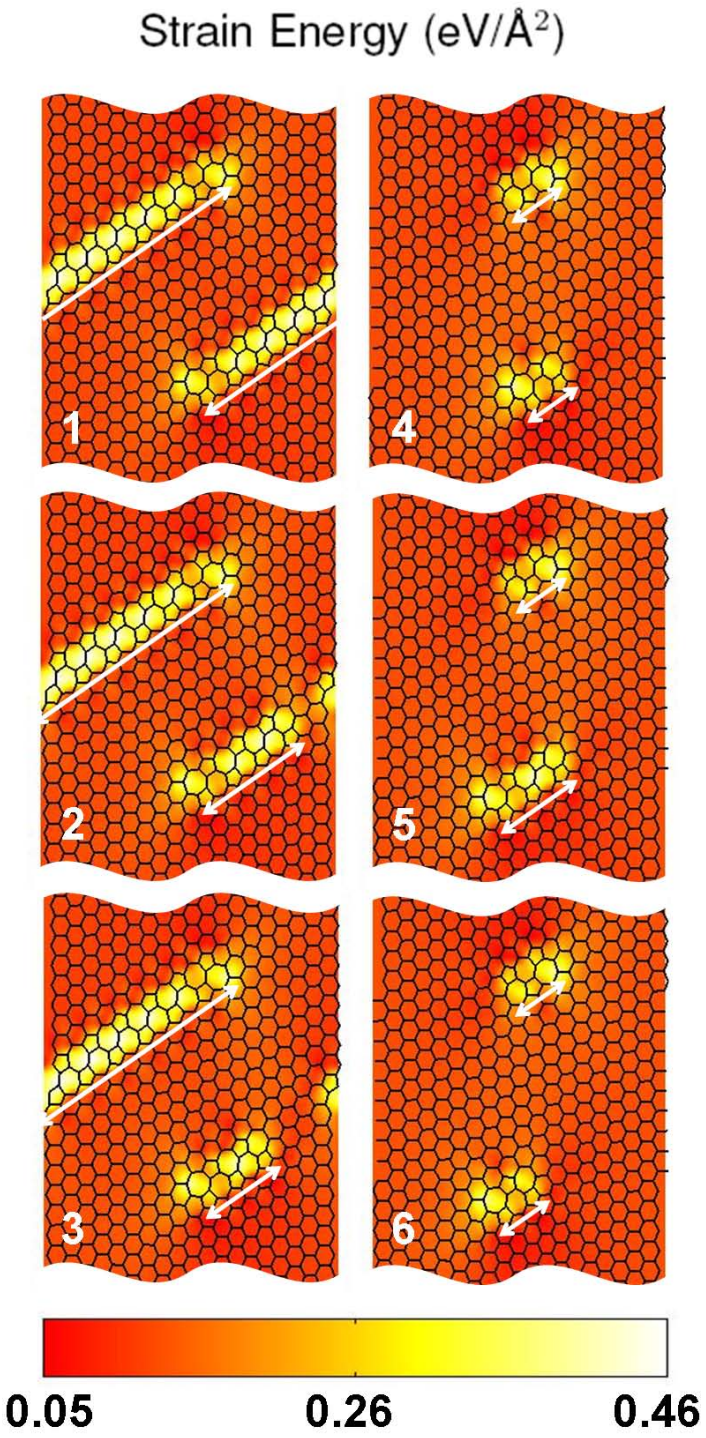

Figure 4.5: Contour plots of strain energy in (10,10) CNTs under high axial stress (1.635 eV/Å^2). The dislocation chains/worms are highlighted by double arrows. Image 1–3 show the breaking of a long dislocation chain From image 3 to panel 4, two short dislocation chains are formed by annihilating several dislocation dipoles. Image 5 and 6 depict the worm-like motion of one chain.

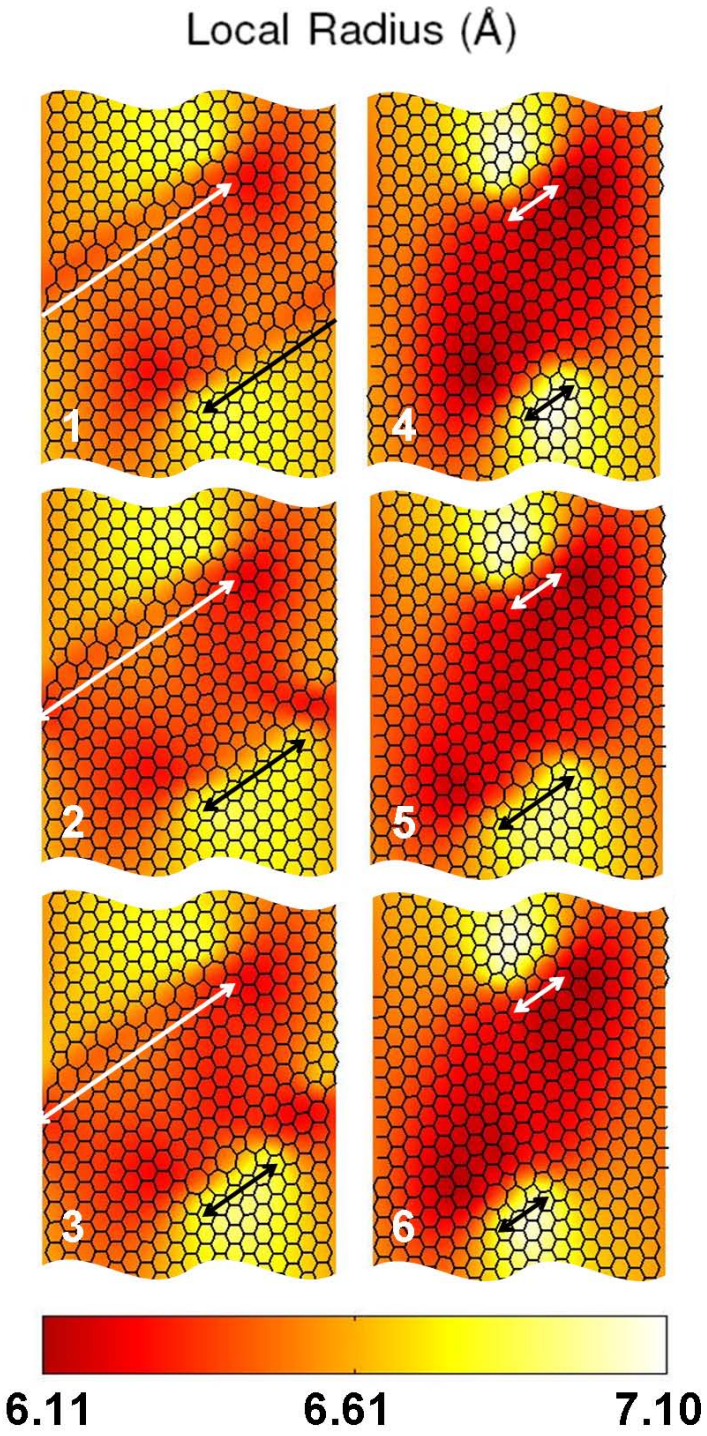

Figure 4.6: Contour plots of local tube radius correspond to Fig. 4.5. A comparison among these plots and those in Fig. 4.4 reveals that isolated dislocations introduce more buckling than dislocation worms.

trailing dipole. In this way, the two dislocation arrays glide away from each other along the slip plane in a cooperative manner, which resembles the motion of a caterpillar or worm and we henceforth refer to the dislocation screened by dipoles as "dislocation worms" (Fig. 4.7).

The appearance of worms at high stress is, at first, puzzling. Within linear elasticity theory, the worms accommodate the same level of plastic strain per step as an isolated dislocation. But in contrast, they have a larger number of dislocation cores, and one expects, a larger net dislocation core energy. This dislocation core energy increase must be balanced by another contribution to the energy.

Examination of two relaxed atomic scale configurations with equivalent plastic strain reveals the source of this additional energy: given equal plastic strain, dislocation glide is associated with a greater level of buckling within the CNT than an array of dislocation dipoles. Isolated defects generated through glide have long–ranged stress fields and consequently high local strain energies (Fig. 4.3). These strain energies can be relieved by buckling that introduces a curvature change in the carbon membrane near the defects at the cost of shortening the tube length, and yielding less macroscopic strain. On the other hand, dislocation worms produce less strain energy than isolated dislocations because the elastic fields of closely packed dislocations are able to effectively screen each other (Fig. 4.5). In this case, less buckling is required to relax strain energies and thus the CNT is shortened less, but the total dislocation core energy increases. At lower stresses, the reduced macroscopic strain is not as costly as the introduction of more dislocation core energies, and glide ensues. At higher stresses, screening dipoles increase the core energy, but enable larger macroscopic strains with each step.

4.3.2 Mechanisms of Plastic Deformation

Since the buckling energy is dependent on the radius of the CNT, it is expected that the worm length is dependent on both the applied stress and the tube radius. In addition, even when screened, the dislocations interact over long ranges. Hence the worm length should also vary as a function of local stresses, the boundary conditions (*e.g.* the imposed periodicity), the total plastic strain, *etc.* To demonstrate this dependence, we construct a plastic deformation map (Fig. 4.8) wherein we identify the number of dislocation dipoles formed during nucleation of individual worms under constant engineering stress conditions with periodic boundary conditions. In addition, Fig. 4.8 identifies regions of the map in which the nanotube simply fails in a brittle fashion (energetically) and shows the yield strength of the armchair CNTs, here defined as the stress for which the formation energy of a Stone-Wales defect is equal to zero.

Several trends emerge. First, larger radii nanotubes lead to a longer chain of dislocation dipoles for a given applied stress. Second, tubes with larger radii display a transition between simple dislocation glide and worm mediated glide at a finite applied stress. Such transitions might be observable using modern microscopy techniques. Third, in the limit of zero mean

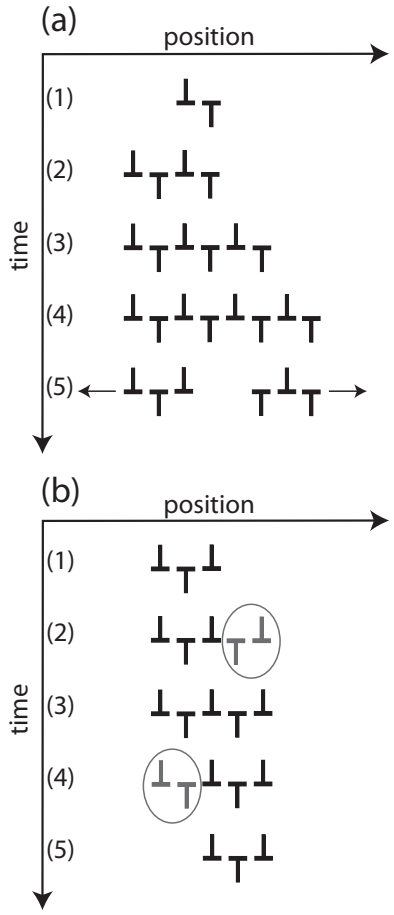

Figure 4.7: (a) An illustration of the nucleation of two worms containing (nominally) three dislocations. At time step (1), a dipole is nucleated. At time (2), a second dipole adjacent to the first is nucleated. Time (3) sees the nucleation of a third dipole pair, and time (4) the fourth. At time (5), the central dipole annihilates, leaving two worms of nominal length three moving the directions shown. This nucleation event would be assigned to region 4 in Fig. 5, because the worm forming structure contains four dipoles. (b) An illustration of the motion of the worm on the right at time (5) in part (a). This worm contains three to five dislocations. At time (1), the worm is in it shortest state. At time (2), the worm begins nucleating a forward dislocation pair(gray, circled). By time (3), the pair is completely formed, and the worm in its longest configuration. At time (4), the trailing dislocation pair begins annihilating (gray, circled). At time (5), the rearward pair has completely annihilated, and the worm is again in its shortest state. The net result is the advancement of the worm by a distance equal to twice the length of the Burgers vector.

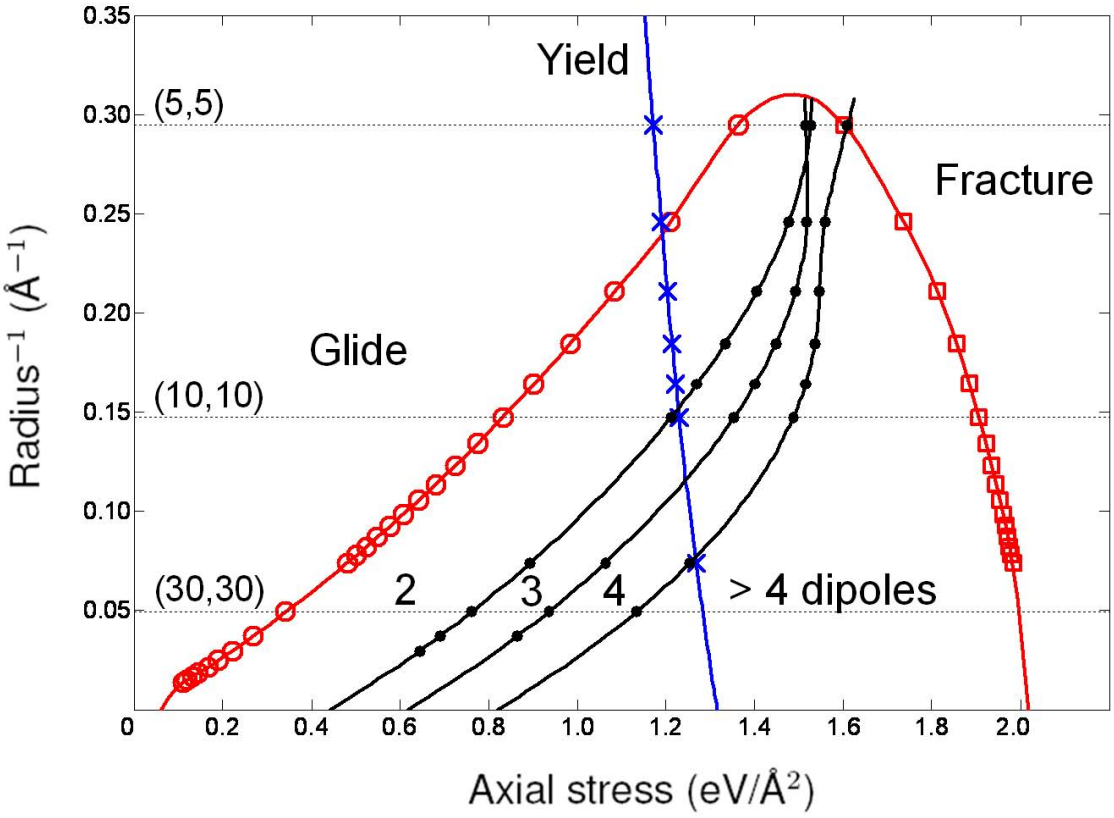

Figure 4.8: The map of plastic deformation mechanisms by tube radius and axial stress for a 85.2 Å long armchair CNT with periodic boundaries. Symbols represent actual calculations, and lines are guides for the eye. In the left region (low stress), dislocation glide is energetically preferred. In middle region, worms are produced from arrays of dislocation dipoles. The number indicates the number of dipoles introduced before it is favorable for the chain to break into two worms. In the right region, CNT's evolve according to the fracture pattern and fail. The yield stress as a function of tube radius is also plotted for reference.

curvature, *i.e.* infinite large radius, the CNT essentially becomes graphene with plasticity, according to the map, dominated by dislocation worms.

We have also conducted total energy electronic structure calculations of various defect configurations in graphene and carbon nanotubes in order to ensure that the patterns emerging from the REBO description persist within more accurate computational methods. The total energy electronic structure calculations reported here are conducted within Density Functional Theory (DFT) [27, 26], employ pseudopotentials [57] and invoke the local density approximation to the exchange correlation energy. Single–particle states are expanded via a plane–wave basis set. The calculated lattice constants and bulk moduli are in good agreement with experimental measurements and other theoretical results, and for each calculation we have ensured convergence with respect to both the k–point mesh and the plane wave cutoff. Tables I and II summarize the results obtained for a (7,7) carbon nanotube (192 atom supercell) and a 180 atom graphene supercell, respectively.

(7,7) Carbon Nanotubes

strain e_{zz}	0%	3.6%	11.0%
Defect Formation Energies from DFT (eV)			
SW	4.05	1.68	-3.48
glide	6.89	3.03	-6.25
worm	7.72	2.80	-7.60
Glide vs. Worm Energy (eV)			
$E_g - E_w$ (DFT)	-0.83	0.23	1.35
$E_g - E_w$ (REBO)	-2.54	-1.04	0.42

Table 4.1: Defect Formation Energies in (7,7) carbon nanotube computed via DFT.

Graphene Sheet

strain e_{zz}	0%	1.9%	8.4%
Defect Formation Energies from DFT (eV)			
SW	4.88	3.87	-0.78
glide	10.09	8.78	0.22
worm	8.99	7.55	-1.81
Glide vs. Worm Energy (eV)			
$E_g - E_w$ (DFT)	1.10	1.23	2.03
$E_g - E_w$ (REBO)	-0.13	0.20	1.15

Table 4.2: Defect Formation Energies in Graphene computed via DFT.

A (7,7) carbon nanotube represented by a 196 atom supercell under tensile loads of 0%, 3.6%, and 11.0% strain was initially considered. In this system, we find that again, worms are favored over glide at high strains where buckling is suppressed (e.g., at 3.6% and 11.0% strain), while as expected, in the unstrained nanotube where buckling is favorable, the formation energy for the isolated dislocation (glide) is lower than that of the worm. By comparison, for the same system now described by REBO, glide is favored for the unstrained and 3.6% strained system, while worms are favored at 11.6% strain. Thus, the trends obtained by the two methods are similar, although in DFT the transition from glide– to worm– mediated deformation takes place at even smaller strains. We also compared the same defect formation energies in a 180 atom graphene sheet at strains of 0%, 1.9%, and 8.4%. In this system, we find that DFT always favors worms over glide for all strains, while REBO does in fact favor glide at 0% strain (although only by 0.13 eV) and then quickly transitions into worm–mediated deformation before 1.9%. Thus, the DFT calculations demonstrate that qualitatively, the patterns described by the REBO description persist, although it appears that DFT favors worm formation over isolated dislocations even more strongly than the empirical potentials (*i.e.*, the transition line between glide and worms in Fig. 4.8 is pushed towards the left).

4.3.3 Plasticity at Finite Temperatures

Finally, we explored the effects of introducing temperature and computed energy barriers for each bond rotation. KMC simulations are used to model a constant engineering stress experiment with a (10,10) armchair CNT (800 atoms and 1200 bonds) loaded with an engineering stress of 1.0 eV/Å^2 ($\sim$ 7.0% initial elastic strain) along the tube axis. The temperature is fixed at 2000 K, below the sublimation temperature of CNT ($\sim$ 2500 K).

Fig. 4.9 and Fig. 4.10 summarize simulation outcomes of 40 runs of the same KMC simulation with different random seeds. At each selected strain, the KMC time data are represented by a box plot [55] where the box shows the 0.25 quartile, the sample median and the 0.75 quartile, and the whiskers indicate the sample minimum and the sample maximum, and plus symbols suggest possible outliers. The initial Stone–Wales defect is nucleated from the defect-free material, taking 81.5 seconds on average (assuming $\nu = 10^{13}$ sec^{-1}), and then the tube elongates rapidly, in accordance with previous results [36]. Along the strain–time curve, some snapshots of the system extracted from a typical KMC run suggest that the plasticity is achieved by a combination of different mechanisms, *e.g.*, dislocation glide, defect nucleation, defect annihilation, *etc.* We note that the formation of dislocation chains persists, even when energy barriers are included, indicating that this plasticity mechanism should in fact occur alongside other mechanisms in experiment. It is also noted that the strain increment from one snapshot to the next is not uniform, although in all cases, the origin is the movement of an edge dislocation by one Burgers vector. If Δe(XY) is used to indicate the strain increment from the snapshot X to Y, then qualitatively we have $\Delta e(\mathrm{BC}) \approx \Delta e(\mathrm{CD}) > \Delta e(\mathrm{AB}) \approx \Delta e(\mathrm{EF}) > \Delta e(\mathrm{DE})$. Interestingly, the process BC or CD

increases a dislocation chain; AB or EF makes a dislocation glide; DE annihilates a defect.

If plasticity is mediated by worms, one might expect this to have an impact on measured properties. For example, the number of slip planes intersected by dislocation cores comprising a single worm is certainly larger than that of isolated dislocations. If dislocations on differing slip planes interact with contact forces, worms will increase the extent of this interaction substantially, possibly yielding an increase in hardening rate.

4.4 Conclusions

In summary, we have developed a phase space sampling approach to study topological defect dynamics in CNTs. We have discovered a new defect pattern, "dislocation worms", that are energetically favored in large CNTs under high axial stresses. In comparison with dislocation glide, dislocation worms lead to less buckling of the carbon membrane and hence allow more effective plastic elongation along the axial direction. More specifically speaking, nanotubes with smaller curvatures are more easy to buckle, which, as discussed in Chapter 3, provides an effective way to reduce the elastic energy of a dislocation dipole. However, such buckling shortens the tube length and therefore decreases the work done of imposed tensile stresses and increases the total energy. It is postulated that the higher the tensile stresses the greater the total energy increase. To explore the strain–time relationship in strain relaxation experiments at finite temperatures, we employ KMC techniques that enable modeling of more realistic time scales by explicitly reflecting computed energy barriers. It is generally true that the nucleation of the first Stone–Wales defect is the strain rate controlling step, and subsequent steps may produce various complicated defect patterns through bond rotations. Some of these patterns are recognized as dislocation worms or dislocation glide.

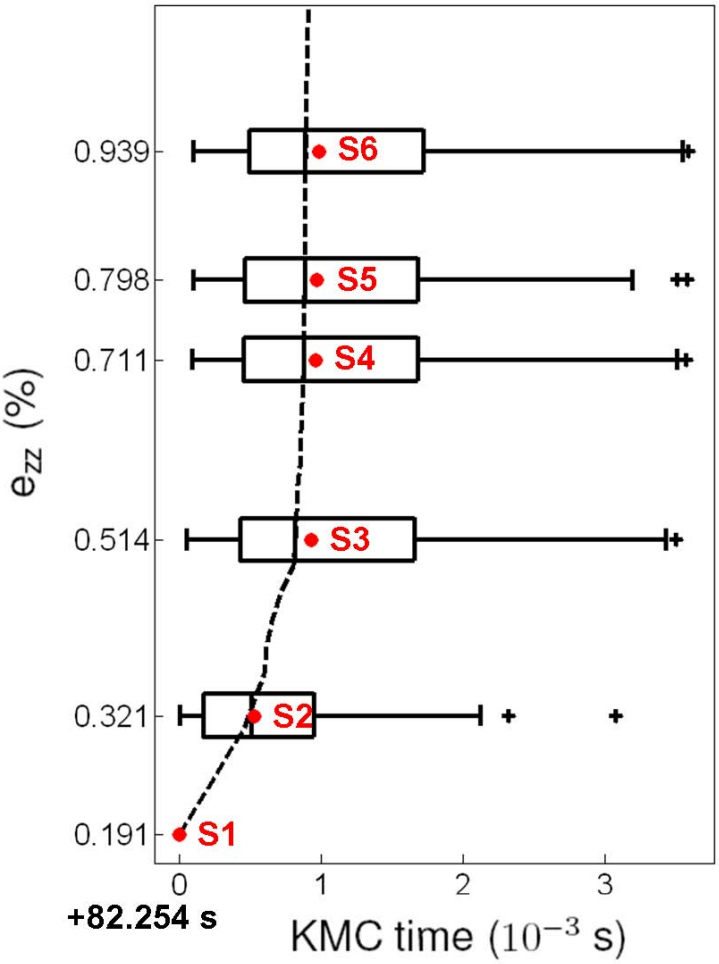

Figure 4.9: The engineering strain versus time curve (dash line) at 2000 K after the formation of an initial Stone–Wales defect. The KMC time data from 40 stochastic independent runs of the same KMC simulation are summarized in box plots. Each box plot depicts the data through the five–number summaries, *i.e.*, the smallest observation, lower quantile, median, upper quantile and largest observation, plus possible outliers.

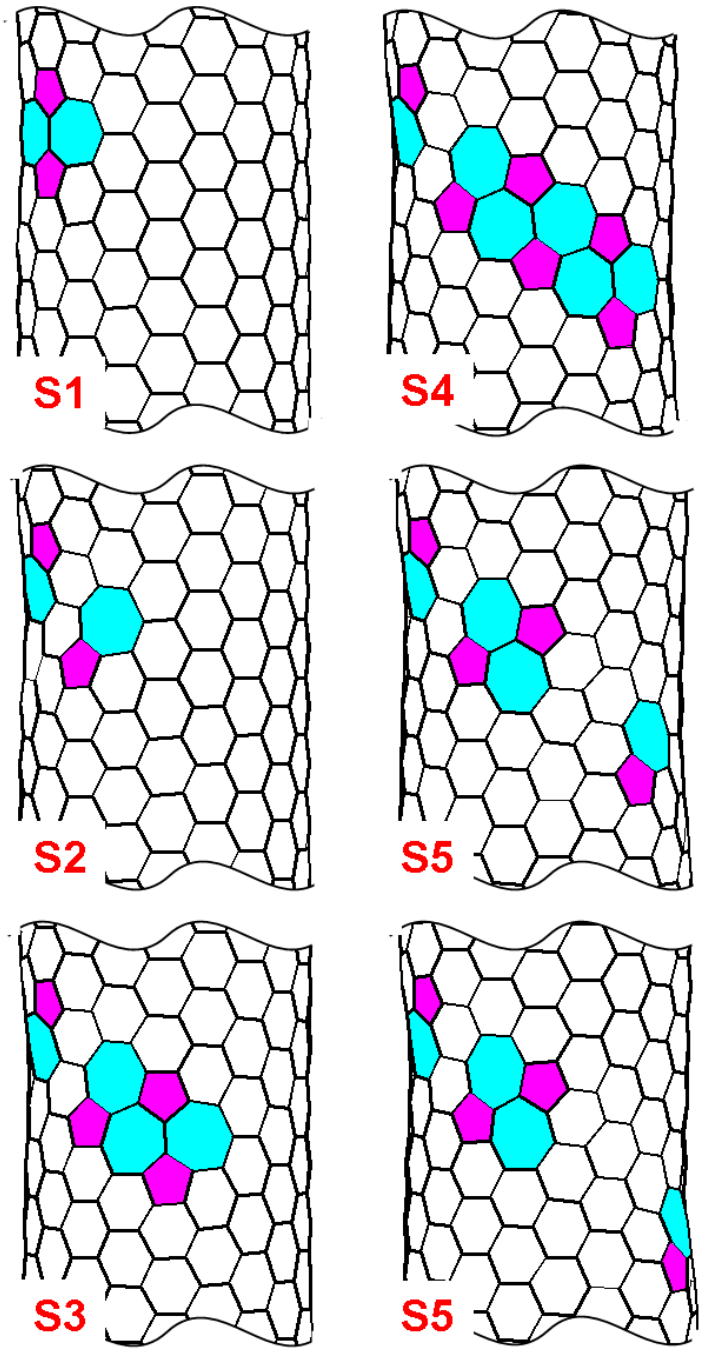

Figure 4.10: Typical snapshots of CNT at several strains in the KMC simulation where image S1–S6 correspond to point S1–S6 in Fig. 4.9. Image S1 shows the nucleation a single SW defect, *i.e.*, an edge dislocation dipole which glides by one step in image S2. In image S3, S4 and S5, a chain of 5 dislocations is formed and then breaks in the middle, leaving a single dislocation in one end. This dislocation then glides in image S6.

Chapter 5

Conclusions

5.1 Key Results and Comments

To understand the elastic properties of free–standing graphene membranes, we employ MC methods within the HtN ensemble which allows rigorous calculations of the elastic compliances and thermal expansion coefficients from fluctuation formulas. Thermal ripples spontaneously develop and their average amplitude increases with the system size, in consistent with the Mermin–Wagner theorem. At high temperatures, the elongation of carbon–carbon covalent bonds expands the graphene membrane, but at the same time the thermal fluctuations effectively folds the membrane, leading to reduced thermal expansion coefficients. In addition, the effective elastic moduli are decreased because an infinitesimal test stress shall easily unfold the crumpled surface instead of stretching many strong sp^2 bonds.

It is very important to realize that in continuum theories of thin plate (for example, the theory developed in Chapter 3), one must use the elastic constants computed in the case when the thermal rippling is manually suppressed [28]. Nevertheless, in real experiments, since thermal rippling always exists, one expects to observe decreased and size dependent elastic properties for a free–standing graphene sheet. Even if the graphene is attached to a substrate, the surface roughness (which may be determined through atomic force microscopy) associated bending strains should be taken into consideration when measuring the elastic moduli.

A transferable, effective but conceptually simple continuum theory is formulated to describe the edge dislocations in graphene or any elastic membranes with periodic boundary conditions. The knowledge of temperature dependent elastic properties of graphene obtained from previous MC simulations provides necessary inputs to the continuum model. The long–range stress field of dislocations puts a flat membrane into a mechanical unstable state which inevitably results in large out–of–plane buckling. The formation energy of a *single* dislocation is then greatly reduced to a constant finite value near 6 eV.

When a graphene sheet is wrapped into a CNT and assuming *no* defect induced buckling,

then the same amount of plastic deformation along the tube axis may be obtaind by gliding a dislocation n steps or creating n Stone-Wales defects forming a "dislocation worm". The former is usually energetically preferred because it introduces less dislocation cores than the latter when $n > 1$. However, the dislocation associated buckling persists and shall shorten the tube length. Geometric relaxations of defected CNTs suggest that the glide pattern generally leads to a shorter tube length than the worm pattern. Notice that under nonzero tensile stresses, a larger plastic elongation corresponds to a greater total energy decrease. Therefore, it is possible that the worm pattern has a lower total energy than the glide pattern as long as the imposed axial tension is large enough to offset the additional defect core energy of the dislocation worm.

5.2 Future Work

Although the classical REBO potential is employed in the MC simulations to understand the elastic properties of graphene, given extra computation resources, it is straightforward to run the same simulations with more sophisticated potentials based on *ab initio* theories in order to obtain more accurate temperature dependent elastic constants. Using our continuum model, it is then easy to calculate the dislocation energy as a function of temperature, a relationship that is tricky to obtain within atomic scale models.

The parallelized KMC algorithm used in Chapter 4 can model the defect dynamics in graphene in a much longer time scale than conventional MD methods, but it is still computation intensive and time consuming. An alternative approach is to combine the KMC technique with the continuum theory. The state of the system can be naturally described by the positions and Burgers vectors of all dislocations as well as the Fourier components of out–of–plane displacements. For simplicity, it may be further assumed that there is no energy barrier for perturbing the membrane surface morphology and the barrier of creating a new dislocation is proportional to the formation energy of this dislocation.

The continuum theory might be extended to compute the buckling of dislocations in CNTs by taking into account the nonlinear terms in the total strain tensor in the cylindrical coordinate system and imposing appropriate topological constraints for dislocations.

Bibliography

[1] W. Bao et al. “Controlled ripple texturing of suspended graphene and ultrathin graphite membranes”. In: Nat. Nanotechnol. 4.9 (2009), pp. 562–566.

[2] E. Bitzek et al. “Structural relaxation made simple”. In: Phys. Rev. Lett. 97.17 (2006), p. 170201.

[3] A. B. Bortz, M. H. Kalos, and J. L. Lebowitz. “New algorithm for monte-carlo simulation of ising spin systems”. In: J. Comput. Phys. 17.1 (1975), pp. 10–18.

[4] D. W. Brenner et al. “A second-generation reactive empirical bond order (REBO) potential energy expression for hydrocarbons”. In: J. Phys. Condens. Matter 14.4 (2002), pp. 783–802.

[5] E. Cerda and L. Mahadevan. “Geometry and physics of wrinkling”. In: Phys. Rev. Lett. 90.7 (2003), p. 074302.

[6] M. S. Daw. “Elasticity effects in electronic structure calculations with periodic boundary conditions”. In: Comput. Mater. Sci. 38.2 (2006), pp. 293–297.

[7] F. Ding et al. “How evaporating CNTs retain their perfection?” In: Nano Lett. 7.3 (2007), pp. 681–684.

[8] F. Ding et al. “Pseudoclimb and dislocation dynamics in superplastic nanotubes”. In: Phys. Rev. Lett. 98.7 (2007), p. 075503.

[9] T. Dumitrica and B. I. Yakobson. “Strain-rate and temperature dependent plastic yield in carbon nanotubes from ab initio calculations”. In: Appl. Phys. Lett. 84.15 (2004), pp. 2775–2777.

[10] T. Dumitrica and B. I. Yakobson. “Strain-rate and temperature dependent plastic yield in carbon nanotubes from ab initio calculations”. In: Appl. Phys. Lett. 84.15 (2004), pp. 2775–2777.

[11] B. R. Eggen et al. “Autocatalysis during fullerene growth”. In: Science 272.5258 (1996), pp. 87–89.

[12] E. Ertekin, D. C. Chrzan, and M. S. Daw. “Topological description of the Stone-Wales defect formation energy in carbon nanotubes and graphene”. In: Phys. Rev. B 79.15 (2009), p. 155421.

[13] E. Ertekin, M. S. Daw, and D. C. Chrzan. "Elasticity theory of topological defects in carbon nanotubes and graphene". In: Philos. Mag. Lett. 88.2 (2008), pp. 159–167.

[14] A. Fasolino, J. H. Los, and M. I. Katsnelson. "Intrinsic ripples in graphene". In: Nat. Mater. 6.11 (2007), pp. 858–861.

[15] P. J. Fay and J. R. Ray. "Monte Carlo simulations in the isoeHtNalpic-isotension-isobaric ensemble". In: Phys. Rev. A 46.8 (1992), pp. 4645–4649.

[16] H. W. Graben and J. R. Ray. "Unified treat. of adiabatic ensemble". In: Phys. Rev. A 43.8 (1991), pp. 4100–4103.

[17] B. I. Halperin and D. R. Nelson. "Theory of 2D melting". In: Phys. Rev. Lett. 41.2 (1978), pp. 121–124.

[18] A. Hashimoto et al. "Direct evidence for atomic defects in graphene layers". In: Nature 430.7002 (2004), pp. 870–873.

[19] J. Y. Huang, F. Ding, and B. I. Yakobson. "Dislocation dynamics in multiwalled carbon nanotubes at high temperatures". In: Phys. Rev. Lett. 100.3 (2008), p. 035503.

[20] J. Y. Huang et al. "Enhanced ductile behavior of tensile-elongated individual double-walled and triple-walled carbon nanotubes at high temperatures". In: Phys. Rev. Lett. 98.18 (2007), p. 185501.

[21] J. Y. Huang et al. "Kink formation and motion in carbon nanotubes at high temperatures". In: Phys. Rev. Lett. 97.7 (2006), p. 075501.

[22] J. Y. Huang et al. "Superplastic carbon nanotubes - conditions have been discovered that allow extensive deformation of rigid single-walled nanotubes." In: Nature 439.7074 (2006), p. 281.

[23] P. Jensen, J. Gale, and X. Blase. "Catalysis of nanotube plasticity under tensile strain". In: Phys. Rev. B 66.19 (2002), p. 193403.

[24] J. W. Jiang, J. S. Wang, and B. Li. "Young's modulus of graphene: A molecular dynamics study". In: Phys. Rev. B 80.11 (2009), p. 113405.

[25] M. Karimi et al. "Elastic constants of silicon using Monte Carlo simulations". In: Phys. Rev. B 58.10 (1998), pp. 6019–6025.

[26] G. Kresse and J. Furthmüller. "Efficiency of ab-initio total energy calculations for metals and semiconductors using a plane-wave basis set". In: Comput. Mater. Sci. 6.1 (1996), pp. 15–50.

[27] G. Kresse and J. Furthmüller. "Efficient iterative schemes for *ab initio* total-energy calculations using a plane-wave basis set". In: Phys. Rev. B 54.16 (1996), pp. 11169–11186.

[28] L. D. Landau and E. M. Lifshitz. Theory of elasticity. Oxford, UK: Pergamon Press, 1986.

[29] A. T. Lee et al. “Reconstruction and alignment of vacancies in carbon nanotubes”. In: Phys. Rev. B 79.17 (2009), p. 174105.

[30] C. Lee et al. “Measurement of the elastic properties and intrinsic strength of monolayer graphene”. In: Science 321.5887 (2008), pp. 385–388.

[31] Z. L. Li et al. “Continuum field model of defect formation in carbon nanotubes”. In: J. Appl. Phys. 97.7 (2005), p. 074303.

[32] P. Liu and Y. W. Zhang. “Temperature-dependent bending rigidity of graphene”. In: Appl. Phys. Lett. 94.23 (2009), p. 231912.

[33] N. D. Mermin and H. Wagner. “Absence of ferromagnetism or antiferromagnetism in one- or two-dimensional isotropic heisenberg models”. In: Phys. Rev. Lett. 17.22 (1966), pp. 1133–1136.

[34] J. C. Meyer et al. “The structure of suspended graphene sheets”. In: Nature 446.7131 (2007), pp. 60–63.

[35] R. S. Millman and G. D. Parker. Elements of differential geometry. Upper Saddle River, NJ: Prentice Hall, 1977.

[36] H. Mori et al. “Energetics of plastic bending of carbon nanotubes”. In: Phys. Rev. B 74.16 (2006), p. 165418.

[37] N. Mounet and N. Marzari. “First-principles determination of the struct., vibr. and thermodyn. properties of diamond, graphite, and derivatives”. In: Phys. Rev. B 71.20 (2005), p. 205214.

[38] T. Mura. Micromechanics of defects in solids. New York, NY: Kluwer Academic, 1987.

[39] M. B. Nardelli, B. I. Yakobson, and J. Bernholc. “Brittle and ductile behavior in carbon nanotubes”. In: Phys. Rev. Lett. 81.21 (1998), pp. 4656–4659.

[40] M. B. Nardelli, B. I. Yakobson, and J. Bernholc. “Mechanism of strain release in carbon nanotubes”. In: Phys. Rev. B 57.8 (1998), R4277–R4280.

[41] M. B. Nardelli, B. I. Yakobson, and J. Bernholc. “Mechanism of strain release in carbon nanotubes”. In: Phys. Rev. B 57.8 (1998), R4277–R4280.

[42] D. R. Nelson. Statistical mechanics of membranes and surfaces. Sinagpore: World Scientific, 2004.

[43] D. R. Nelson and L. Peliti. “Fluctuations in membranes with crystalline and hexatic order”. In: J. Phys. 48.7 (1987), pp. 1085–1092.

[44] B. Peng et al. “Measurements of near-ultimate strength for multiwalled carbon nanotubes and irradiation-induced crosslinking improvements”. In: Nat. Nanotechnol. 3.10 (2008), pp. 626–631.

[45] J. R. Ray. “Fluctuations and thermodynamics properties of anisotropic solids”. In: J. Appl. Phys. 53.9 (1982), pp. 6441–6443.

[46] J. R. Ray and A. Rahman. "Statistical ensembles and molecular dynamics studies of anisotropic solids". In: J. Chem. Phys. 80.9 (1984), pp. 4423–4428.

[47] G. G. Samsonidze, G. G. Samsonidze, and B. I. Yakobson. "Energetics of Stone-Wales defects in deformations of monoatomic hexagonal layers". In: Comput. Mater. Sci. 23.1-4 (2002), pp. 62–72.

[48] H. S. Seung and D. R. Nelson. "Defects in flexible membranes with crystalline order". In: Phys. Rev. A 38.2 (1988), pp. 1005–1018.

[49] P. Spellucci. "A new technique for inconsistent QP problems in the SQP method". In: Math. Methods Oper. Res. 47.3 (1998), pp. 355–400.

[50] P. Spellucci. "An SQP method for general nonlinear programs using only equality constrained subproblems". In: Math. Program. 82.3 (1998), pp. 413–448.

[51] M. Sternberg et al. "Carbon Ad-dimer defects in carbon nanotubes". In: Phys. Rev. Lett. 96.7 (2006), p. 075506.

[52] A. J. Stone and D. J. Wales. "Theoretical studies of icosahedral C_{60} and some related species". In: Chem. Phys. Lett. 128.5-6 (1986), pp. 501–503.

[53] K. Suenaga et al. "Imaging active topological defects in CNTs". In: Nat. Nanotechnol. 2.6 (2007), pp. 358–360.

[54] C. Tang, W. Guo, and C. Chen. "Molecular dynamics simulation of tensile elongation of carbon nanotubes: temperature and size effects". In: Phys. Rev. B 79.15 (2009), p. 155436.

[55] J. W. Tukey. Exploratory data analysis. Reading, MA: Addison-Wesley, 1997.

[56] G. Van Lier et al. "Ab initio study of the elastic properties of single-walled carbon nanotubes and graphene". In: Chem. Phys. Lett. 326.1-2 (2000), pp. 181–185.

[57] D. Vanderbilt. "Optimally smooth norm-conserving pseudopotentials". In: Phys. Rev. B 32.12 (1985), pp. 8412–8415.

[58] Y. P. Varshni. "Temperature dependence of the elastic constants". In: Phys. Rev. B 2.10 (1970), pp. 3952–3958.

[59] D. C. Wallace. Thermodynamics of crystals. Mineola, NY: Dover Publications, 1998.

[60] Y. W. Wong and S. Pellegrino. "Wrinkled membranes part II: analytical models". In: J. Mech. Mater. Struct. 1.1 (2006), pp. 27–61.

[61] B. I. Yakobson. "Mechanical relaxation and "intramolecular plasticity" in carbon nanotubes". In: Appl. Phys. Lett. 72.8 (1998), pp. 918–920.

[62] K. V. Zakharchenko, M. I. Katsnelson, and A. Fasolino. "Finite temperature lattice properties of graphene beyond the quasiharmonic approximation". In: Phys. Rev. Lett. 102.4 (2009), p. 046808.

[63] Q. Z. Zhao, M. B. Nardelli, and J. Bernholc. "Ultimate strength of carbon nanotubes: a theoretical study". In: Phys. Rev. B 65.14 (2002), p. 144105.

[64] Q. Z. Zhao, M. B. Nardelli, and J. Bernholc. "Ultimate strength of carbon nanotubes: a theoretical study". In: Phys. Rev. B 65.14 (2002), p. 144105.